Influences of CAPE on Hail Production in Simulated Supercell Storms

YUZHU LIN[a] AND MATTHEW R. KUMJIAN[a]

[a] *Department of Meteorology and Atmospheric Science, The Pennsylvania State University, University Park, Pennsylvania*

(Manuscript received 24 February 2021, in final form 21 October 2021)

ABSTRACT: Lasting updrafts are necessary to produce severe hail; conventional wisdom suggests that extremely large hailstones require updrafts of commensurate strength. Because updraft strength is largely controlled by convective available potential energy (CAPE), one would expect environments with larger CAPE to be conducive to storms producing larger hail. By systematically varying CAPE in a horizontally homogeneous initial environment, we simulate hail production in high-shear, high-instability supercell storms using Cloud Model 1 and a detailed 3D hail growth trajectory model. Our results suggest that CAPE modulates the updraft's strength, width, and horizontal wind field, as well as the liquid water content along hailstones' trajectories, all of which have a significant impact on final hail sizes. In particular, hail sizes are maximized for intermediate CAPE values in the range we examined. Results show a non-monotonic relationship between the hailstones' residence time and CAPE due to changes to the updraft wind field. The ratio of updraft area to southerly wind speed within the updraft serves as a proxy for residence time. Storms in environments with large CAPE may produce smaller hail because the in-updraft horizontal wind speeds become too great, and hailstones are prematurely ejected out of the optimal growth region. Liquid water content (LWC) along favorable hailstone pathways also exhibits peak values for intermediate CAPE values, owing to the horizontal displacement across the midlevel updraft of moist inflow air from differing source levels. In other words, larger CAPE does not equal larger hail, and storm-structural nuances must be examined.

KEYWORDS: Supercells; Hail; Numerical analysis/modeling

1. Introduction

Hail annually causes billions of dollars in agricultural and property damage, both in the United States and abroad, accounting for more than half of all severe weather–related economic or insured losses, as well as injuries or casualties in many regions (Guan et al. 2015; Kahraman et al. 2016; Gunturi and Tippett 2017). Additionally, damages caused by individual hailstorms can sometimes exceed hundreds of millions of dollars, depending on the size and quantity of hailstones, and the location of the hail swath (e.g., Picca and Ryzhkov 2012; National Weather Service-San Antonio 2016; Kunz et al. 2018). Therefore, knowledge of the types of storm environments that can produce severe hail is important.

Compared to small hail, large hail can be especially dangerous for homes, automobiles, livestock, and humans. As such, the U.S. National Weather Service includes the occurrence of severe hail (≥1 in. or 25.4 mm in maximum dimension) in the warning criteria for severe thunderstorms. However, the prediction of hail size remains a challenge owing to the limitations of observation and detection methods (Blair et al. 2011, 2017; Ortega 2018), as well as current convection-allowing models (Gagne et al. 2017; Adams-Selin et al. 2019). Given these challenges, near-storm soundings and quantities derived from them such as CAPE and low- or midlevel lapse rates, or radar-derived indices such as severe hail index (SHI) and maximum estimated size of hail (MESH; Witt et al. 1998) are often used in operational forecasting and detection of hail size (e.g., National Weather Service WDTB 2021).

There have been many attempts to investigate how storm environments influence hail size by examining the relationship between reported hail size and representative sounding-derived parameters or bulk severe weather indices. For example, using the Storm Prediction Center (SPC) reports database, WSR-88D radar observations, and soundings, Edwards and Thompson (1998) find no significant relationship between hail size and CAPE, environmental freezing level (FZL), vertically integrated liquid water (VIL), maximum parcel level, equilibrium level, convective cloud depth, wet-bulb zero level (WBZ), or any combinations among them. Jewell and Brimelow (2009) draw data from a high-density hail observer network and find a large overlap between the CAPE values associated with storms that produce hailstones larger and smaller than 2 in. (50 mm), as well as a negative relationship between hail size and surface-based parcel buoyancy (and subsequently the strength of the updraft). Johnson and Sugden (2014) use a quality-controlled NCDC storm report database (*Storm Data*) and Rapid Update Cycle (RUC) model to create a parameter-based hail climatology. Similar to Edwards and Thompson (1998), they find little skill for FZL and WBZ, along with most unstable lifting condensation level (MULCL) in discriminating hail size. The mean values of most unstable CAPE (MUCAPE), mean-layer CAPE (MLCAPE), and 700–500-hPa lapse rate increase slightly alongside neighboring hail size categories, but their distributions exhibit large overlaps. Johnson and Sugden (2014) also develop the large hail parameter (LHP) and find it, along with the significant severe parameter (SSP; Craven and Brooks 2004), as better discriminators between size categories

Supplemental information related to this paper is available at the Journals Online website: https://doi.org/10.1175/JAS-D-21-0054.1.s1.

Corresponding author: Yuzhu Lin, yxl5930@psu.edu

DOI: 10.1175/JAS-D-21-0054.1

compared to all aforementioned parameters. Further, they find a wind profile with greater veering and stronger deep-layer shear to be potentially favorable for large hail. By examining hail events across Europe using the European Severe Weather Database (ESWD) and proximity soundings, Púčik et al. (2015) draw similar conclusions on MUCAPE and deep-layer shear; however, they also find an increased LCL height associated with higher possibilities for severe hail, echoing the results of Groenemeijer and van Delden (2007) and Kaltenböck et al. (2009). Blair et al. (2017), using data from the Hail Spatial and Temporal Observing Network Effort (HailSTONE) and the WSR-88D radar network, suggest that storm mode and organization have a strong influence on hail size. In particular, they find that supercell storms tend to produce the largest hailstones, which supports the previous findings by Nelson (1983), Rasmussen and Blanchard (1998), Thompson et al. (2003), Blair et al. (2011), Duda and Gallus (2010), and Smith et al. (2012), among many others. Taszarek et al. (2020) compare hail-producing convective environments over Europe and the contiguous United States using a combination of the SPC reports database, ESWD, and the fifth-generation ECMWF reanalysis (ERA5; Hersbach et al. 2020). They find that CAPE and effective shear are notably larger for events that produce hailstones ≤ 5 cm compared to non-severe thunderstorms in both the United States and Europe, despite the overlap between neighboring hail-size categories. Additionally, sounding-derived composite indices developed for use in the United States, such as the significant hail parameter (SHIP) and supercell composite parameter (SCP), show weakened performance in Europe. WMAXSHEAR (Taszarek et al. 2017), a parameter similar to SSP, appears to be similarly applicable in both areas. The lack of definitive results stemming from these studies points to both the complexity of hail production and the biases in hail databases (e.g., Jewell and Brimelow 2009; Allen and Tippett 2015; Blair et al. 2017; Ortega 2018).

Others take an alternate approach by examining the "ingredients" and physical processes behind simulated hail growth in three-dimensional storm environments; many of these studies highlight the importance of storm flow fields (e.g., Paluch 1978; Heymsfield et al. 1980; Conway and Zrnić 1993; Kennedy and Detwiler 2003). Early works such as Nelson (1983); Miller and Fankhauser (1983), and Foote (1984), using storm flow fields and environmental conditions retrieved from multi-Doppler radar networks and soundings, find that hailstones grow during a single pass through the updraft. Further, they find that optimal hail growth is achieved when hailstones are of a size such that they are nearly balanced by the updraft and do not experience strong upward excursions and/or exit the updraft prematurely, whether through its top or its sides. This implies that a broad, moderate updraft in the prime hail growth region can be a key factor for determining hail size. Foote (1984) also suggests that the largest hailstones usually result from embryos entering through the southwest corner of a supercell's updraft,[1] because they can travel the full length of the updraft's long dimension following its cyclonic flow field. This points to the importance of horizontal flow and storm morphology, a conclusion supported by Nelson (1987) and others (e.g., Miller et al. 1988; Tessendorf et al. 2005; Dennis and Kumjian 2017; Kumjian and Lombardo 2020). Dennis and Kumjian (2017, hereafter DK17) explore how variations in the storm flow field influence hail growth by systematically altering the environmental vertical wind shear in numerical simulations with a fixed thermodynamic profile and producing a series of varying supercell storms. Using output from the two-moment Morrison microphysics scheme (Morrison et al. 2005, 2009), DK17 find that an increased deep-layer zonal wind shear can lead to greater hail mass produced. The increased hail production results from an elongation of the storm's updraft in the zonal direction and a subsequent increased volume of the optimal hail growth region, increased hailstone residence times within the updraft, and broadening of the potential embryo source regions. Increased low-level meridional shear, on the other hand, results in smaller hail mass, which they attribute to a separation of hypothetically favorable embryo source regions and the actual locations of available embryos. Kumjian and Lombardo (2020, hereafter KL20) elaborate on these results following a similar approach by varying vertical wind shear, but develop and use a detailed explicit microphysical hail growth trajectory model instead of output from the bulk microphysics parameterization scheme. They suggest that the decrease of hail size produced by storms with large low-level meridional shear results from faster southerly flow within the updraft, which rapidly advects hailstones through the optimal hail growth region, resulting in shorter residence times despite the elongation of the updraft's north–south dimension. These studies reveal additional complexity, in that a storm's flow field, as opposed to singular features such as the updraft strength or size, influences residence time during hail growth and thus modulates hail size. Therefore, it is unsurprising that bulk parameters such as CAPE or deep-layer shear—which do not capture such nuances—often fail as forecasting tools.

CAPE is commonly employed as a proxy for instability available to storms, as well as their updraft strength. Although it is widely recognized that large CAPE- or, a strong updraft-alone is not the sole requirement for storms to produce large hail, it is still used in hail research and forecasting. For instance, Renick and Maxwell (1977) attempt forecasting maximum hail size in the Alberta Hail Project area based upon a direct, nomogramic comparison of modified maximum updraft velocity, and the temperature at which it occurs between upcoming storms (calculated using a one-dimensional (1D) loaded moist adiabatic model described in Chisholm and English (1973)) and past reports. The original 1D HAILCAST model, developed and improved by Poolman (1992), Brimelow et al. (2002), and Jewell and Brimelow (2009), employs CAPE in calculating the energy shear index (a product of CAPE and 850-hPa 6-km bulk wind shear), which is used to estimate the lateral and cloud-top entrainment applied to the storm's updraft, as well as the storm's lifetime. The storm's lifetime, along with the storm's updraft strength (which is also a function of CAPE), is then used in determining hailstones' residence time and therefore their

[1] For supercells in the Northern Hemisphere.

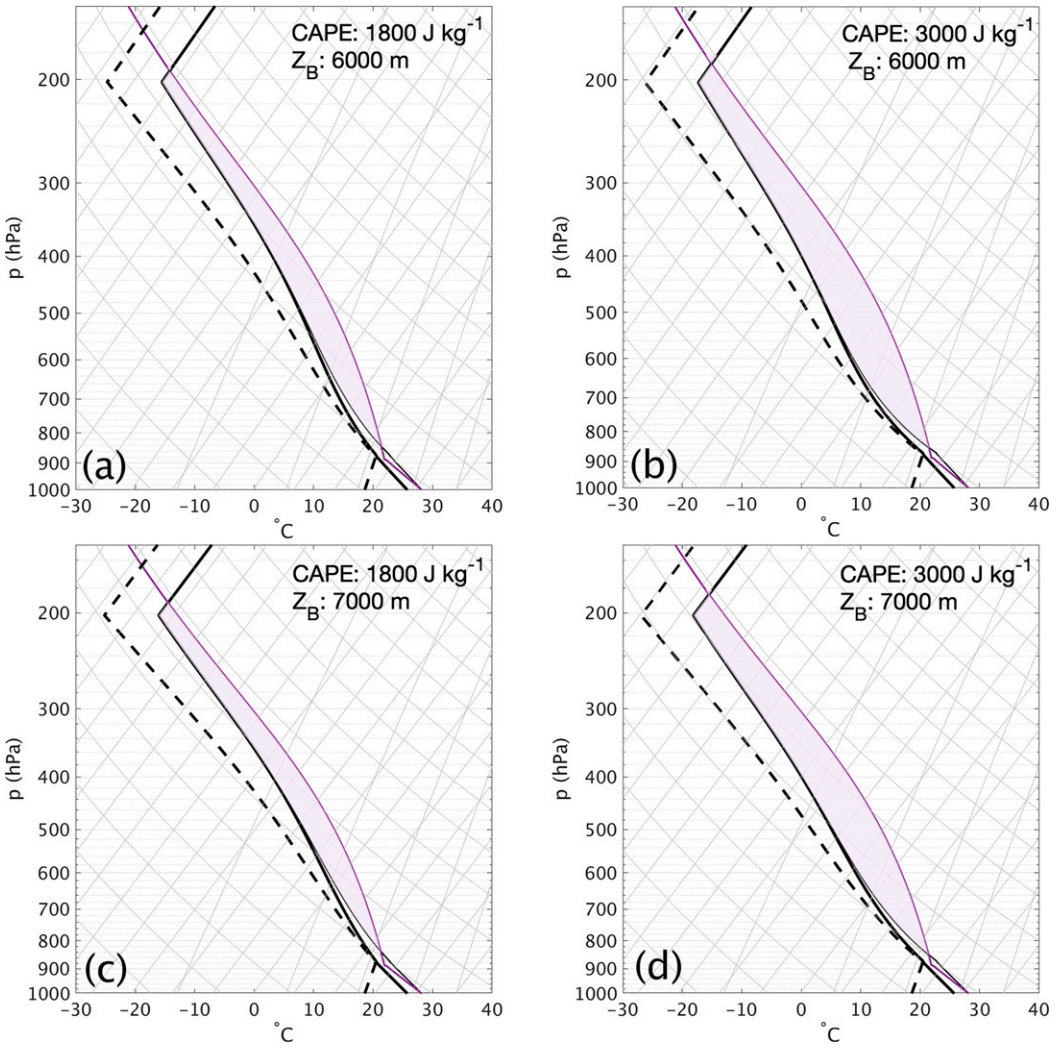

FIG. 1. (a)–(d) Skew T–log$p$ diagrams showing examples of idealized base-state thermodynamic profiles. Dashed black lines represent the dewpoint temperature, and thick solid black lines represent the temperature. Thin solid black lines indicate the virtual temperature of the environment, and the thin solid purple lines indicate the path of an air parcel rising adiabatically from the surface to the LCL and pseudoadiabatically thereafter. Shaded areas represent positive buoyancy. The corresponding CAPE (J kg^{-1}) and Z_B values (m) are listed in each panel.

final sizes. HAILCAST shows improvement over the nomogram method in correctly forecasting on hail size categories. These efforts place major focus on a 1D representation of the storm's vertical structure, where updraft strength and duration is directly modulated by CAPE. Thus, these studies suggest a positive correlation between CAPE and hail size. Adams-Selin and Ziegler (2016) modify HAILCAST by using a time-dependent updraft speed multiplier to characterize the horizontal advection of hailstones across the updraft upon its implementation to Weather Research and Forecasting (WRF) Model (Skamarock et al. 2008). Combined with larger embryo sizes, this updraft multiplier improves forecast accuracy for hailstones $>$ 25 and $>$50 mm. CAPE is also used in some climatologies for estimating hail size (e.g., Manzato 2003, 2012, 2013).

A notion exists that, since larger hailstones are associated with greater terminal velocity (Khvorostyanov and Curry 2002; Mitchell and Heymsfield 2005; Morrison et al. 2015; Heymsfield et al. 2018), if all other conditions (e.g., LWC, vertical shear) remain equal, lasting supercell storms in environments with larger CAPE produce increased hail size as a result of their strong updraft. The stronger updraft allows storms to "hold up" these hailstones—meaning they need to stay suspended in an updraft with vertical velocity larger than their terminal velocity for a considerable amount of time compared to the hailstones' growth span. However, this argument lacks credibility because hailstones can continually collect mass and grow in size as they fall through the hail growth region (e.g., Rasmussen and Heymsfield 1987; KL20). Further, the growth during their descent can be significant,

u_{max} (m s^{-1}) \ Z_B (km)	6.5	7.0	7.5	8.0
25		1500, 1600, ...2700 J kg^{-1}		
31	1800, 2000, ...3000 J kg^{-1}	1800, 1900, ...3000 J kg^{-1}	1800, 2000, ...3000 J kg^{-1}	1800, 2000, ...3000 J kg^{-1}
36		1800, 1900, ...3000 J kg^{-1}		

FIG. 2. Summary of numerical simulations. The left column indicates the u_{max} value for the hodograph (m s^{-1}). The top row indicates the level of maximum buoyancy Z_B (km). Each cell contains the list of different CAPE values (J kg^{-1}) used. Increments are implied by the first two values listed. The green-shaded box represents the varying CAPE (u31_z7) experiments; the red-shaded boxes represent the varying deep-layer shear (z7) experiments; the blue-shaded boxes represent the buoyancy profile experiments.

because hailstones would already be larger in size (i.e., larger effective collection area) from their initial ascent and growth, and the probability of appreciable supercooled liquid water mass increases with increasing temperatures (e.g., Pruppacher and Klett 1997). Nonetheless, CAPE is known to modify storm structure, updraft morphology, and the storm's flow field (McCaul and Weisman 2001; Kirkpatrick et al. 2011; Peters et al. 2019, 2020a), which are key factors in modulating hail production. Yet, the extent to which variations in CAPE influence hail size has yet to be thoroughly tested or quantified.

Here, we aim to investigate how CAPE influences hail growth in supercell storms by conducting a model-based parameter space study. A summary of the methods employed in designing and performing numerical simulations is described in section 2. Section 3 contains results. Section 4 includes discussion and summary of the study, as well as implications for future research.

2. Methods

Simulations of idealized supercell storms are conducted using Cloud Model 1 (Bryan and Fritsch 2002), version 18.3. The simulations are three-dimensional, with a domain width of 75 km on each side and depth of 20 km. The grid spacing is 500 m horizontally and 250 m vertically. Rayleigh damping is performed in the upper 5 km of the domain. The domain moves at a constant speed during each simulation following the storm movement to keep the midlevel updraft core at its center, so that the edge of each storm's updraft is kept at least 20 km from the edge of the domain. As such, the horizontal winds shown and discussed here are in the storm-relative reference frame. The bottom and top boundaries are free-slip and the lateral boundaries are open-radiative. A vertically implicit Klemp–Wilhelmson time-splitting scheme (Klemp and Wilhelmson 1978) is employed as the pressure solver for temporal integration. The Morrison two-moment microphysics scheme (Morrison et al. 2005, 2009) is used with hail set as the default "large-ice" category for high-density riming, although hail growth-related output produced by the microphysics scheme is not directly used for our analysis.

Storms are initiated by a warm bubble with a 1-K potential temperature perturbation in a horizontally homogeneous environment. The base state consists of a "quarter-circle" wind profile (Weisman and Rotunno 2000) and an idealized input thermodynamic profile described below.

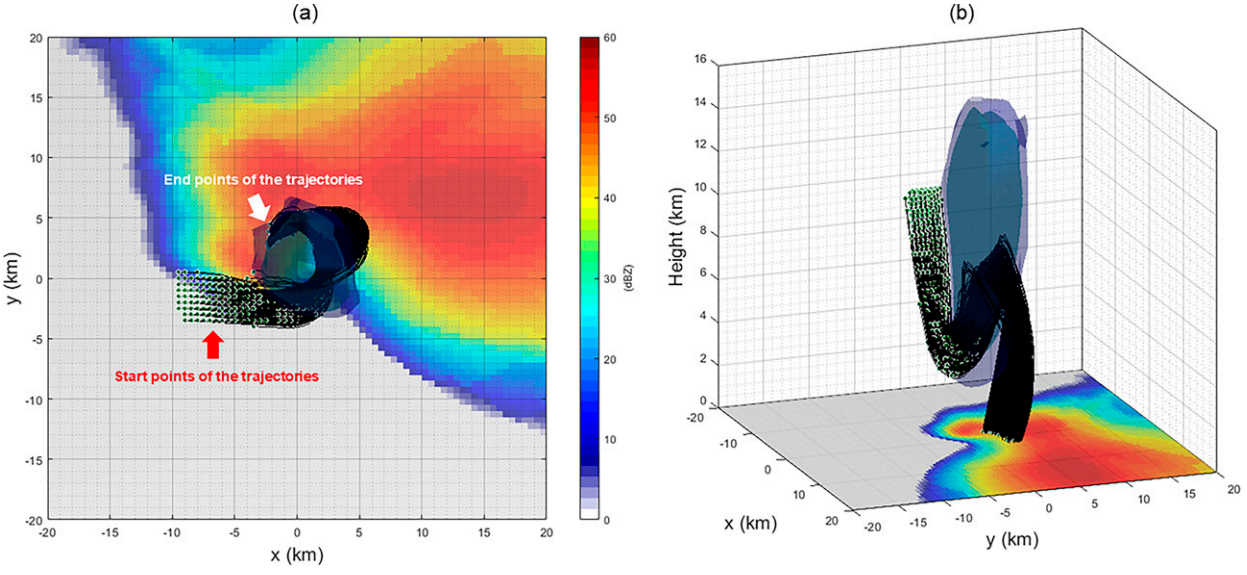

FIG. 3. (a) Top view and (b) three-dimensional view toward the west-northwest of hailstone trajectories (black lines) through the simulated supercell updraft in u31_z7_2400. The updraft isosurfaces of 20 and 30 m s^{-1} are shown in blue shading. The bottom of each panel shows the simulated reflectivity factor (shaded according to scale; dBZ). The hailstone trajectories feature an arching, northward path through the growth region.

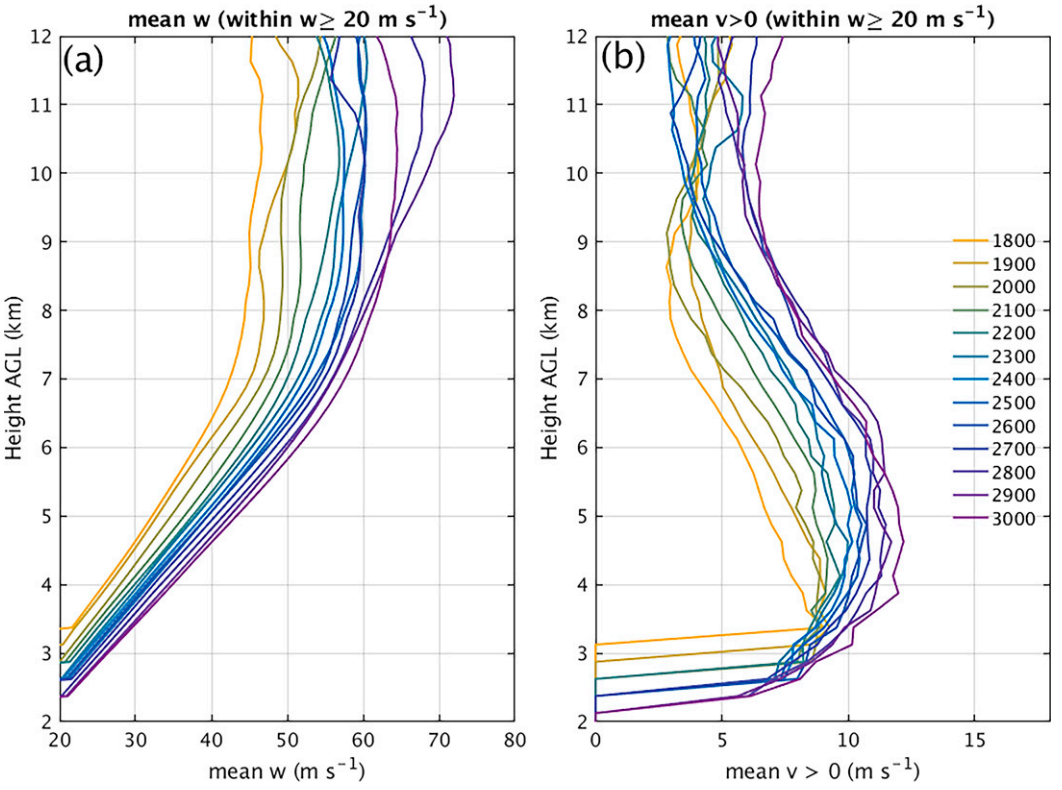

FIG. 4. Vertical profile of (a) the mean upward velocity ($w > 0$) and (b) the mean southerly horizontal wind ($v > 0$) in the u31_z7 simulations, both conditionally averaged within the updraft $w \geq 20$ m s^{-1}. Each line represents a different simulation with the environmental CAPE value (J kg^{-1}) given according to the legend. Increasing CAPE values correspond to cooler colors.

Variations in the shear magnitudes for the quarter-circle hodographs are chosen from DK17 to cover a range of observed supercell storm environments (e.g., Marwitz 1972; Brooks et al. 1994). These hodographs are constructed such that the southerly ($v > 0$) wind component reaches its maximum v_{max} = 7 m s^{-1} at 2 km AGL, whereas the westerly ($u > 0$) wind component reaches 7 m s^{-1} at 2 km AGL and its maximum value u_{max} of 25, 31, or

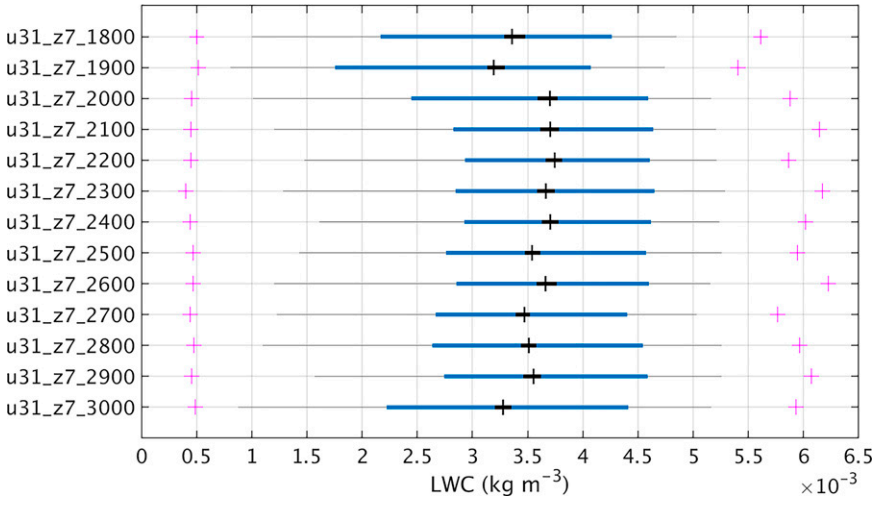

FIG. 5. Distribution of LWC values (kg m^{-3}) within the 20 m s^{-1} updraft in the hail growth region (between 4 and 8 km AGL) for the u31_z7 simulations. Boxes show the 25th–75th percentile (interquartile) range, and whiskers show the 10th and 90th percentiles. The vertical bar within the box is the median value, with the black bar indicating its 5th and 95th percentile confidence levels. The magenta marks indicate the maximum and minimum LWC for each case.

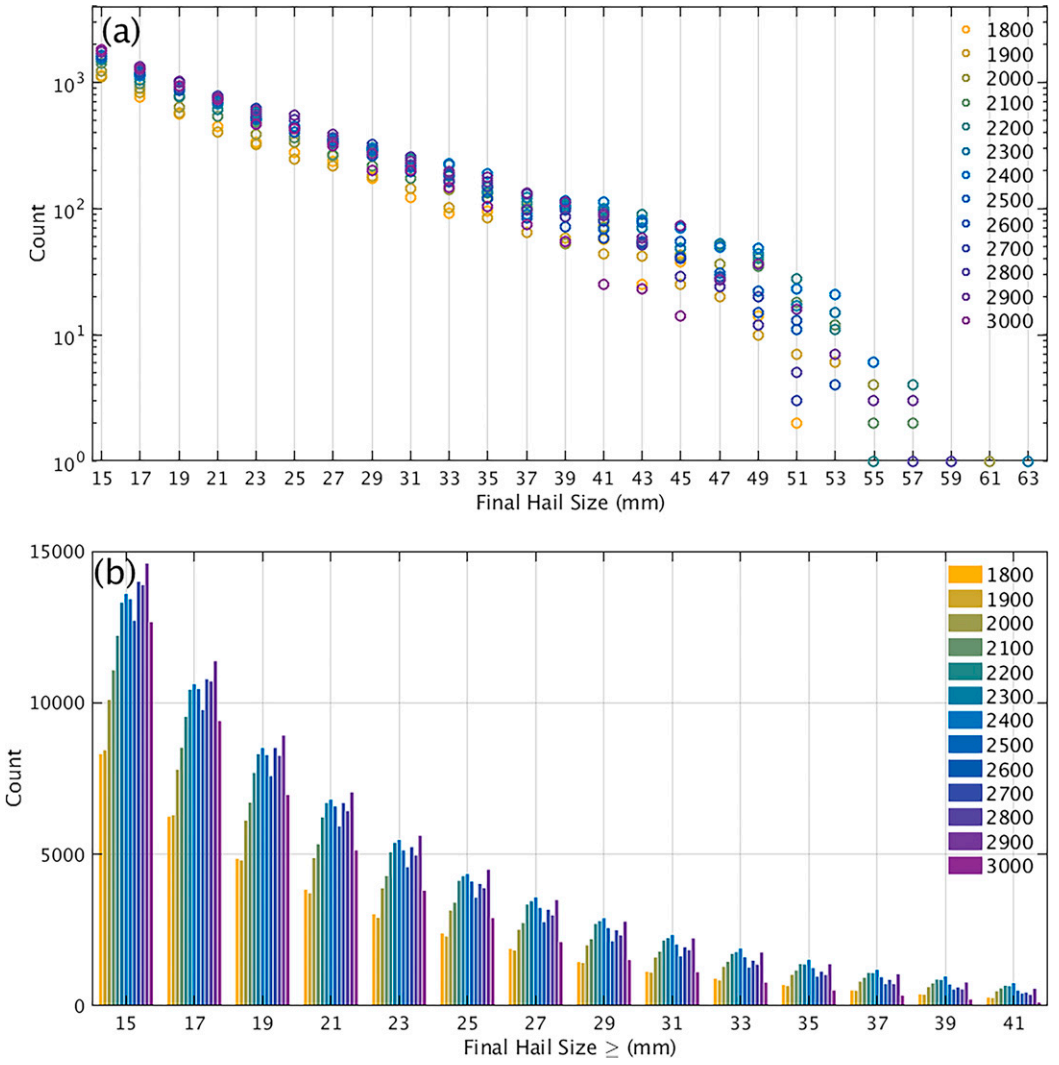

FIG. 6. Number of embryos that produce hailstones (a) in different size bins and (b) with diameters larger than given thresholds in u31_z7 simulations. The environmental CAPE value (J kg^{-1}) in each case is given according to the legends; increasing CAPE values correspond to cooler colors. In (b), bars from left to right indicate increasing CAPE.

36 m s^{-1} at 6 km AGL for the u25, u31, and u36 cases, respectively. The initial thermodynamic conditions are constructed using the same method as McCaul and Weisman (2001) and Warren et al. (2017), which allows for systematic adjustment of the buoyancy profile, thereby enabling experiments with controlled CAPE and vertical buoyancy distributions. Key values such as pressure and height are prescribed for the surface, mixed-layer top, and tropopause, and are described in Table 1. Relative humidity H_Z (%) in the free troposphere is specified by a predefined function of height:

$$H_Z = H_{\mathrm{ML}} - \frac{(H_{\mathrm{ML}} - H_{\mathrm{TP}})(Z - Z_{\mathrm{ML}})}{(Z_{\mathrm{TP}} - Z_{\mathrm{ML}})^{1.5}}, \tag{1}$$

where H represents relative humidity and Z represents height. Subscripts ML and TP represent values at the mixed-layer top and tropopause, respectively. All other symbols are defined in Table 1. Buoyancy in the free troposphere is defined as $B_z = g(T_{v,p} - T_{v,e})/T_{v,e}$ and is constructed as a function of Z, CAPE (denoted by E), and the level of maximum buoyancy Z_B:

$$B_Z = E\frac{Z - Z_{\mathrm{ML}}}{(Z_B - Z_{\mathrm{ML}})^2}\exp\left(-\frac{Z - Z_{\mathrm{ML}}}{Z_B - Z_{\mathrm{ML}}}\right), \tag{2}$$

where g is the gravitational constant, $T_{v,e}$ is the environmental virtual temperature and $T_{v,p}$ is the virtual temperature of an air parcel rising pseudoadiabatically from the surface. Other thermodynamic variables are then calculated from the given parameters.

By systematically varying CAPE and Z_B, we produce a series of idealized initial thermodynamic conditions (Fig. 1). Base-state profile configurations for all supercell simulations, including thermodynamic conditions and wind shear

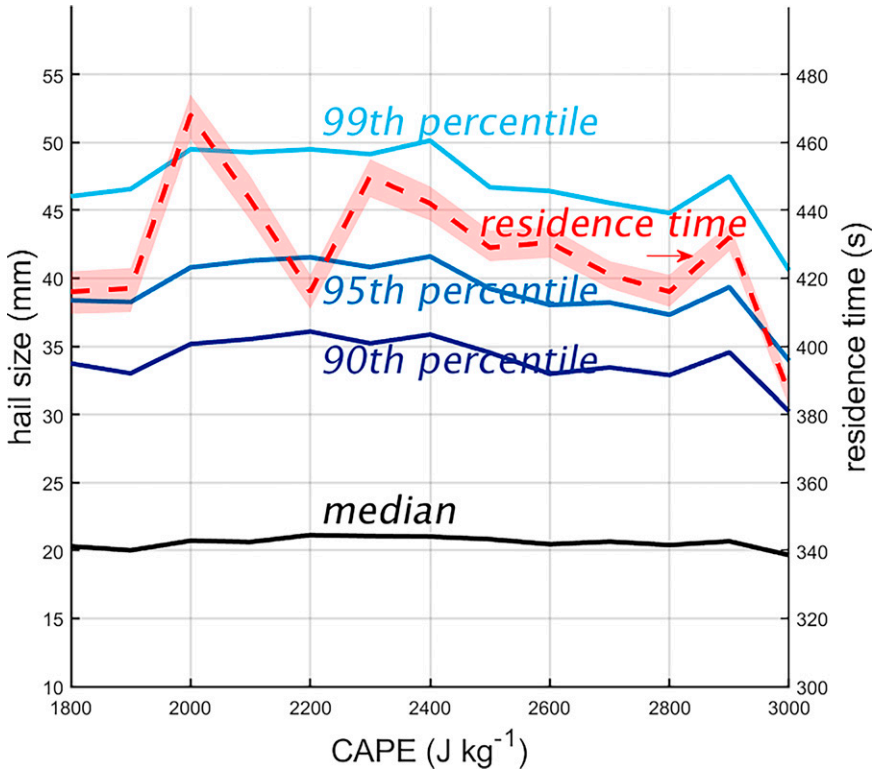

FIG. 7. Different hail size metrics (averaged over all embryo sizes) as a function of CAPE value in the u31_z7 simulations, conditionally sampled for ≥15 mm are the solid lines: black for the median, dark blue for the 90th percentile, blue for the 95th percentile, and cyan for the 99th percentile. Note the "peak" or optimal CAPE values around 2000–2400 J kg^{-1}. The dashed red line is the composite median residence time (s; displayed on the right ordinate axis) of different seeding sizes within the 20 m s^{-1} updraft for hailstones attaining final sizes ≥ 15 mm in diameter. The shaded bands about each line indicate the 95% confidence interval about the median values.

magnitudes, are presented in Fig. 2. It is worth noting that the parameter space we choose represents typical high-shear, high-CAPE supercell storms occurring in the contiguous United States, although supercells, marginal supercells, and nonsupercell storms with relatively low CAPE values are also capable of producing large hailstones (Brooks 2013; Sherburn and Parker 2014; Púčik et al. 2015; Taszarek et al. 2020). Therefore, our results may not necessarily apply to all hail-producing environments. The naming convention for each simulation follows a format of shear, level of maximum buoyancy, and surface-based CAPE: for example, a simulation where u_{max} = 31 m s^{-1}, Z_B = 7 km, and CAPE = 1800 J kg^{-1} is referred to as u31_z7_1800. A complete set of simulations with varying CAPE and a fixed shear magnitude and level of maximum buoyancy will be referred to only by their shared parameters, such as u31_z7. Each simulation runs for 2 h with a 1-s time step, and produces output files every 5 min. We then composite each resulting right-moving supercell storm over the second simulated hour with a method similar to Grant and van den Heever (2014), DK17, and KL20. The grid point with maximum updraft speed at midlevels (7 km AGL) is found for each output time and set as the new domain center, where simulation results are then composited into a single 50 km × 50 km × 20 km 3D data field for the hail trajectory simulations, centered at x = 0 km, y = 0 km, z = 0 km.

The hail trajectory calculations are performed using the hail growth trajectory model by KL20. The model accounts for important microphysical processes relevant for hail growth along in-storm trajectories by advecting initial hail embryos across the 3D input wind, moisture, and thermodynamics fields produced by CM1 using a 1-s time step, performing microphysical calculations on each hailstone and outputting their size, mass, location, and fall speed, among other properties. In this study, initial embryos with a density of 917 kg m^{-3} are placed in a 24 × 24 × 7.5 km^3 "seeding cube" centered at x = 2 km, y = 2 km, z = 7.125 km in the model domain. The horizontal spacing for neighboring embryos is 500 m and the vertical spacing is 250 m. For each idealized storm input, the hail growth trajectory model runs four separate times with embryo diameters of 2.5, 5.0, 7.5, and 10.0 mm, respectively, producing four different sets of outputs. The hail statistics presented in the results section is a numerical average between all four outputs.

Sensitivity tests on model resolution with a horizontal grid spacing of 250 m and a vertical grid spacing of 250 m are performed with selected CAPE values. Simulations with a finer

TABLE 1. Key variables used to specify the idealized thermodynamic base-state profiles.

Variable	Definition (units)	Value
P_S	Surface pressure (hPa)	1000
Z_{ML}	Mixed-layer depth (km)	1
P_{ML}	Pressure at mixed-layer top (hPa)	880
T_{ML}	Temperature at mixed-layer top (K)	290
H_{ML}	Relative humidity at mixed-layer top (%)	95
Γ_{ML}	Lapse rate for potential temperature in mixed layer (K km^{-1})	1
Z_{TP}	Tropopause depth (km)	12
H_{TP}	Relative humidity at the tropopause (%)	25

resolution produce slightly larger hailstones, with the 50th, 90th, 95th, and 99th hail size percentiles increasing <2 mm compared to that of our base simulations, but the relationship between CAPE and hail size (see following sections) remains the same (see the supplemental material).

3. Results and analysis

The homogeneous base states in all 60 simulations develop long-lasting, deep moist convection triggered by warm bubbles. During each run, the initial singular convective cell splits into two separate storms (left- and right-moving supercell storms) within the first simulated hour. The left-moving storms are less structured than the right-moving storms, and usually exhibit signs of becoming multicellular due to our choice of hodograph (Weisman and Rotunno 2000; Markowski and Richardson 2010; Warren et al. 2017). Storm structures and microphysical properties of the right-moving storm differ with varying CAPE, Z_B, and 0–6-km vertical wind shear. To respectively investigate the influence of each environmental quantity on hail production, we divide our analysis into three sections: u31_z7 experiments with only CAPE variations, z7 experiments with varying shear for each CAPE value to examine how the results for u31_z7 simulations are modulated with changes to deep-layer shear, and u31 experiments with varying Z_B for each CAPE value to examine how the vertical distribution of buoyancy affects the results (Fig. 2). To ensure the updraft morphology stays consistent for each experiment, we choose a lower range of CAPE for u25_z7 simulations to prevent the early weakening and decay of existing cells.

a. u31_z7 experiments

To investigate CAPE's influence on hail production, we first conduct u31_z7 experiments where only CAPE varies between each CM1 simulation (the "green box" in Fig. 2). For all base states, u_{max} = 31 m s^{-1}, and Z_B = 7 km AGL. CAPE ranges between 1800 and 3000 J kg^{-1}, in 100 J kg^{-1} increments. This variation of CAPE is expected to have a wide range of impacts on storm properties, of which the in-storm wind field and supercooled liquid water content are expected to be of the greatest significance for hail production (e.g., English 1973; Heymsfield et al. 1980; Nelson 1983; Ziegler et al. 1983; Foote 1984; Rasmussen and Heymsfield 1987, among many others). The structure and magnitude of the storm wind field can directly modulate hailstones' residence time, during which they can remain in the updraft's optimal hail growth region (roughly between 4 and 8 km AGL for our simulations), where the environment is rich in supercooled liquid water (cloud droplets and raindrops) and thus provides adequate liquid mass for hailstones to collect.

In these simulated right-moving supercell storms, our calculations show favorable hailstone trajectories are the paths that move primarily northward within the updraft (Fig. 3), consistent with the archetypal trajectory proposed by Browning and Foote (1976) and those seen in our recent work (DK17; KL20; Kumjian et al. 2021). As such, we mainly consider the southerly ($v > 0$) component of the horizontal wind within the updraft, which is important for advecting particles across the updraft during growth, as well as the updraft speed itself,

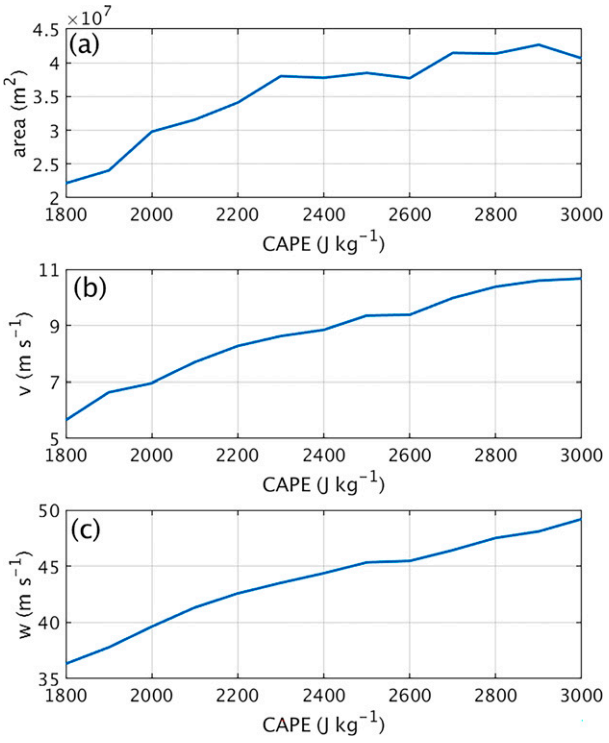

FIG. 8. Changes in (a) mean updraft area between 4 and 8 km AGL, (b) mean southerly ($v > 0$) wind speed, and (c) mean $w > 0$, all sampled within the 20 m s^{-1} updraft between 4 and 8 km AGL, as a function of CAPE for the u31_z7 simulations.

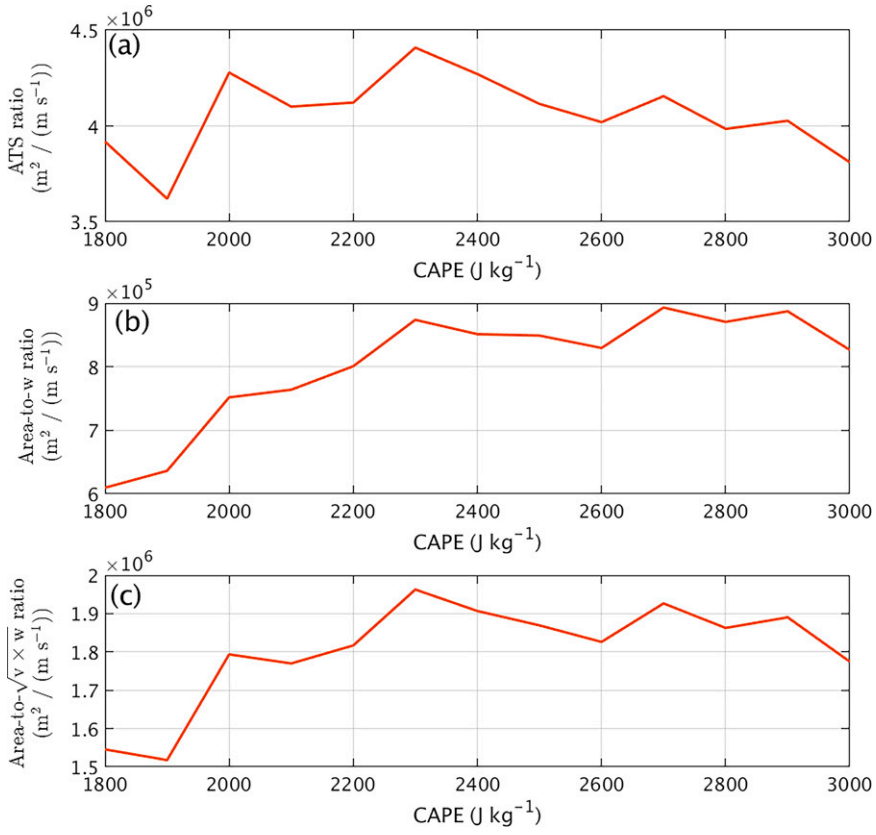

FIG. 9. Changes in (a) updraft area-to-southerly wind (ATS) ratio, (b) updraft area-to-mean vertical velocity ratio, and (c) updraft area-to-mean-$\sqrt{w \times v}$ ratio, for the u31_z7 simulations, conditionally sampled on $w \geq 20$ m s^{-1} between 4 and 8 km AGL. Units for each ordinate axis are m^2 (m s^{-1})$^{-1}$.

which is important for supporting a growing hailstone's vertical excursions as its fall speed increases with mass relative to the vertical wind (further details for examining these two variables will be discussed later in this section). Figure 4 shows the vertical profiles of upward vertical velocity and storm-relative southerly horizontal wind within the updraft for each composited storm. Increases in CAPE, while other environmental conditions remain unchanged, tend to increase both the average upward and southerly wind speed within the updraft below 10 km AGL.

Changes in CAPE inevitably influence the amount and distribution of liquid water in storms, as well. Here, the LWC is defined as the sum of the cloud droplet and raindrop mass mixing ratios multiplied by dry air density. The LWC distribution within the $w \geq 20$ m s^{-1} updraft and confined to the 4–8 km AGL hail growth region for each right-moving storm composite is shown in Fig. 5 to home in on the region relevant for hail growth. Even though the updraft LWC in all varying-CAPE experiments covers a similar interquartile range, the median LWC values are maximized for some "optimal" CAPE values between 2000 and 2400 J kg^{-1}, where the median LWC is the greatest compared to cases where CAPE values are either smaller or larger; the reasons behind this will be discussed in detail below.

How do these storm structural changes influence hail production? As discussed above, one might expect the amount of severe hail and the maximum hail size produced to increase with CAPE, given CAPE is correlated to maximum updraft speed (e.g., Weisman and Klemp 1982; Rasmussen and Blanchard 1998; Markowski and Richardson 2010; Peters et al. 2020a). However, results produced by the hail growth trajectory model show no significant correlation between CAPE and either hail attribute: the simulated hail size metrics for the u31_z7 experiments, averaged between four initial embryo sizes, are shown in Fig. 6. The distribution of final sizes illustrated in Fig. 6a reveals that the number of embryos that grow into hailstones ≥ 15 mm decreases exponentially as hail size increases in each simulation, in line with previous results in KL20. Notably, however, there is more variability in the "tail" end of the distribution for larger hail sizes, in part because of the lower counts (i.e., rarer occurrence) of these larger stones. Thus, we expect differences in other metrics related to the larger hail sizes. Figure 6b shows the number of initial embryo seeds resulting in a size greater than or equal to that shown on the abscissa. A similar pattern can be identified for all size thresholds: although the relationship between number of small hail and CAPE is overall positive, the number of hailstones with sizes > 25 mm increases with increasing

CAPE from 1800 to about 2400–2500 J kg^{-1}. Beyond that peak value, however, the counts exhibit a non-monotonic behavior, with a secondary peak at about 2900 J kg^{-1}. This is clearly seen in Fig. 7, which shows different hail size metrics conditionally sampled for hailstones ≥ 15 mm as a function of CAPE. Note the "optimal" value of CAPE (shown as a broad peak in hail metrics) seems to be in the ~2000–2400 J kg^{-1} range, with another peak at 2900 J kg^{-1}. The non-monotonic behavior indicates a complex hail production dependence on CAPE for these simulations. In essence, in our idealized supercell environments, increasing CAPE, though leading to stronger updrafts, does not necessarily lead to increased hail sizes. The increase in hail sizes for 2900 J kg^{-1} CAPE is because of new hail growth pathways opened in the storm: increased storm-relative winds outside of the updraft (arising owing to the storm motion farther from the hodograph) combined with larger updraft area helps expand the region where embryos can be swept into the updraft and achieve significant growth (not shown). However, hail-resulting embryo regions in other u31_z7 experiments show similar spatial patterns. This points to other differences in the hail growth ingredients arising from variations in CAPE alone.

We next look at residence time, because the increase of residence time for larger CAPE serves as a main argument for the idea that large CAPE is beneficial for producing large hail. The dashed line in Fig. 7 shows the median residence time within the 20 m s^{-1} updraft in the hail growth region for hailstones grown to be ≥15 mm, composited between different seeding sizes and presented as a function of CAPE. Positive correlations exist between different hail size metrics and the median residence time (the linear correlation coefficient ρ for 50th, 90th, 95th, and 99th percentile hail size and median residence time is 0.652, 0.732, 0.775, and 0.817, respectively), meaning the distribution of final hail sizes shifts to larger values with increasing residence time, as expected (e.g., Heymsfield 1983; Foote 1984, KL20). Similar to hail size, median hail residence time does not increase monotonically with increasing CAPE, but instead exhibits a relative maximum ~2000–2400 J kg^{-1} and minor peaks at 2600 and 2900 J kg^{-1}.

To understand how CAPE influences hailstones' residence time, we look back at the other determining factors related to hailstone trajectories within the updraft: the updraft area and updraft's horizontal wind field. Residence time is expected to increase as the storm's updraft area grows. This is because a larger updraft area would enable a greater number of embryos to enter the hail growth region as potential seedings for large hail production, as well as longer pathlengths as hailstones are advected across the updraft (e.g., Nelson 1983; Ziegler et al. 1983; DK17; KL20). Hail residence time also benefits from more moderate horizontal wind speed, because it slows hailstone advection through the updraft and prevents hailstones from being prematurely ejected out of the hail growth region before achieving significant growth (e.g., KL20).

The change of updraft area, magnitude of the southerly wind component, and updraft strength with varying CAPE is shown in Fig. 8. The vertical velocity within the storm's hail

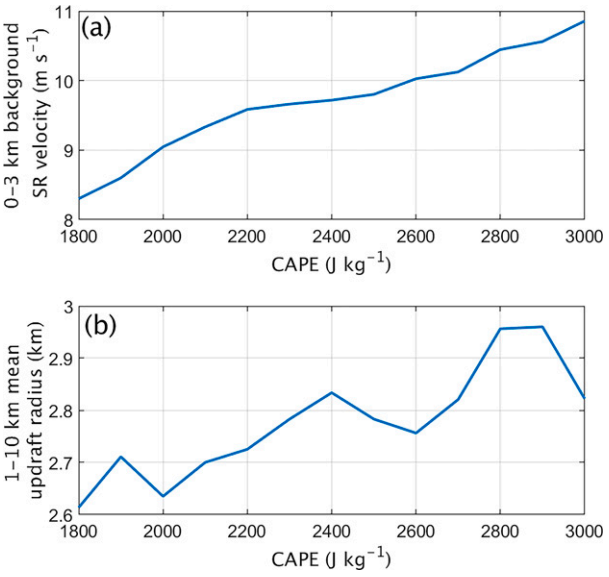

FIG. 10. Relationship between CAPE and (a) mean 0–3-km storm-relative wind (m s^{-1}), and (b) 1–10-km mean 3 m s^{-1} updraft radius (km) for the u31_z7 simulations, only accounting for the right-moving storms.

growth region increases with CAPE, as expected; the storm's updraft area within the hail growth region also expands with increased CAPE, as shown in previous studies (McCaul and Weisman 2001; Kirkpatrick et al. 2011; Markowski and Richardson 2010; Peters et al. 2019), contributing to a longer residence time if all other variables remain equal. However, the horizontal wind speed within the same updraft area *also increases* with CAPE (Fig. 8b), competing against the increase in updraft area and contributing to a shorter residence time. To examine the outcome of this competition, a simple ratio of updraft area to southerly wind speed (ATS ratio hereafter) is calculated. A larger ATS ratio means a potentially larger residence time given the longer possible pathlengths and slower advection speed. As a corollary, smaller ATS ratio values imply shorter pathlengths and/or faster advection speeds, suggesting smaller residence times and less favorable growth. The ATS–CAPE relationship (Fig. 9a) is significantly and positively correlated to the residence time–CAPE relationship shown in the dashed red line in Fig. 7 ($\rho = 0.799$), suggesting that ATS ratio can be used as a proxy for residence time. Figure 9b features the ratio of mean updraft area to mean vertical velocity, and Fig. 9c shows the ratio of mean updraft area to the mean $\sqrt{w \times v}$ value, which compares the significance of horizontal wind speed and the traditionally used vertical velocity in modulating hailstones' excursions. Both quantities are calculated within the hail growth region. The ATS ratio, out of all three, best correlates with residence time; it is also significantly correlated to 50th, 90th, 95th and 99th hail size percentiles discussed above (ρ = 0.839, 0.685, 0.669, 0.637, respectively). The other two ratios show no significant correlation, except for the ratio of mean updraft area to the mean $\sqrt{w \times v}$ value and 50th hail size percentile ($\rho = 0.594$).

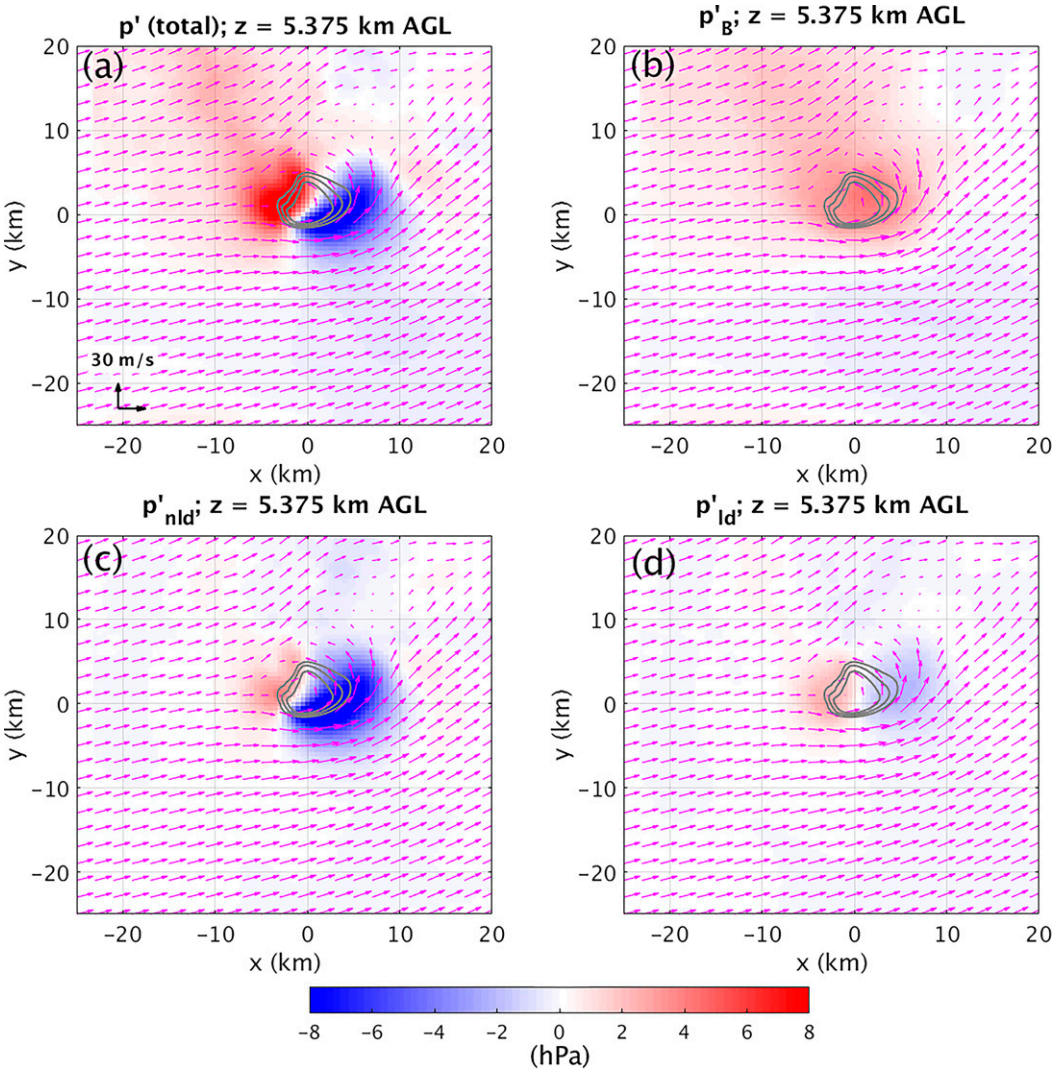

FIG. 11. Horizontal slices through the u31_z7_2400 storm at 5.375 km AGL, showing the (a) total pressure perturbation, shaded according to scale (Pa), and contributions to it from the (b) buoyancy, (c) nonlinear dynamic, and (d) linear dynamic terms, calculated using MUDPACK (Adams 1999). The magenta vector field represents the storm's horizontal wind field, whereas the gray lines are the updraft 20, 25, and 30 m s^{-1} contours.

What causes the increase in both updraft area and southerly flow speed with larger CAPE? We know that updraft area is increased with greater deep-layer shear, which tends to increase the magnitude of the low-level storm-relative winds (e.g., DK17; Trapp et al. 2017; Warren et al. 2017; Peters et al. 2019; KL20). For these u31_Z7 experiments, deep-layer shear is fixed. All 13 simulated storms move northeast throughout their lifetimes, but those in environments with larger CAPE are associated with a smaller northward component and a larger eastward component to this motion. Thus, the resulting motion is farther away from the uniform quarter-circle hodograph used, so storms with larger CAPE experience stronger low-level storm-relative winds, which is associated with wider updrafts (e.g., Peters et al. 2019, 2020a). Further substantiation is offered by a comparison between our simulations and the data provided in Peters et al. (2019). In our simulations, the mean 0–3-km storm-relative wind magnitudes increase from 8.3 to 10.9 m s^{-1} when CAPE increases from 1800 to 3000 J kg^{-1} (Fig. 10a). Based on their Figs. 4a and 5a, the 1–10-km average effective updraft radius R_{eff} should have an approximate change from 4.0 to 4.8 km, an increase of 20%; our calculated 1–10-km average updraft radius increases to 2.96 from 2.61 km or 13.2% (Fig. 10b), which is quite consistent.

The low-level storm-relative wind magnitude also is strongly positively correlated to the storm's average low-level inflow speed, defined as the horizontal speed of the low-level air being advected toward the updraft's boundary (Peters et al. 2019). Indeed, one might expect these larger inflow speeds with increasing CAPE to play a role in the

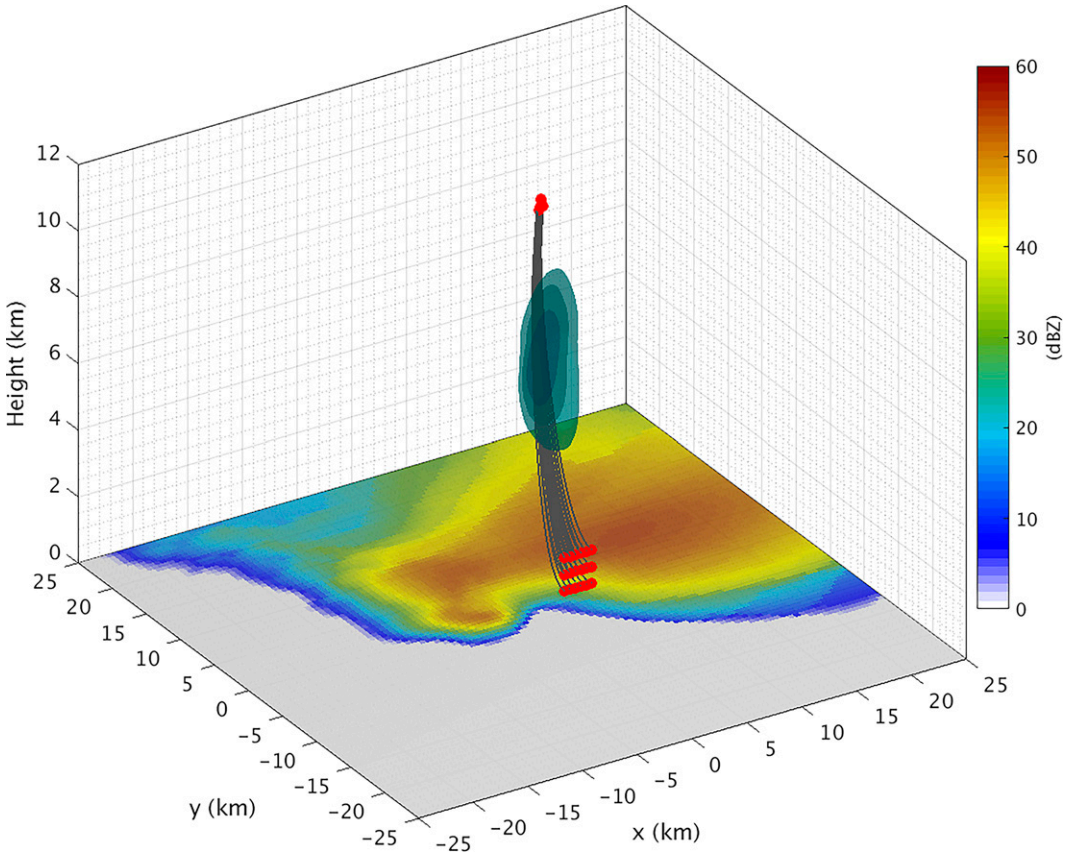

FIG. 12. Three-dimensional view of the 15 air parcels used in the calculations. The red circles indicate the starting and ending points of the air parcels, and the gray lines are their trajectories. The isosurfaces of pressure perturbations −3.5, −4.0, and −4.5 hPa are shown. The simulated reflectivity factor (dBZ, according to scale) is underlaid.

larger southerly wind within the updraft further aloft, beause air in the storm's updraft largely comprises air rising from the inflow layer (Nowotarski et al. 2020). In the same pressure field, parcels with greater horizontal momentum entering the updraft at low levels are expected to retain greater horizontal momentum further aloft in the hail growth region. However, the variation in the average southerly wind speed within the hail growth region is larger than that of the average inflow speed: when CAPE increases from 1800 to 3000 J kg^{-1}, the average inflow speed increases by ~2 m s^{-1}, whereas the average southerly wind speed within the hail growth region increases by nearly 5 m s^{-1} (Fig. 8b). This suggests that the difference lies not only in air parcels' initial horizontal momentum, but other factors are also affecting the parcel's behavior during its approach and ascent into the updraft. Air parcels from the inflow layer that ultimately participate in the updraft are lifted by buoyancy and vertical perturbation pressure gradient forces (e.g., Markowski and Richardson 2010; Peters 2016). Further, the air parcels' horizontal speeds are influenced by the storm's horizontal perturbation pressure gradient force (Dahl 2017). Particularly in supercells, these pressure perturbations may be large, leading to appreciable horizontal acceleration of the ascending parcels by the pressure gradient field.

Figure 11 depicts the storm's buoyancy, dynamic, and overall pressure perturbation fields. A negative pressure perturbation exists at the southern part of the updraft between 4 and 10 km AGL mainly owing to the strong nonlinear dynamic pressure deficit resulting from the "spin" term associated with vertical vorticity (see, e.g., Markowski and Richardson 2010). This negative pressure perturbation accelerates inflow air parcels as they head northward, meaning the v component of the inflow wind will increase before reaching the negative pressure perturbation's center. Similarly, once rising parcels advance northward past the negative pressure perturbation center, they experience an adverse horizontal perturbation pressure gradient force and decelerate.

To quantify the impact of the negative pressure perturbation region on the horizontal airspeed of parcels entering the optimal hail growth region, we perform a simple air parcel experiment (Fig. 12). For this experiment, 15 air parcels were initialized in the inflow region (defined as the southeast quadrant of the domain at heights < 3 km AGL). We choose to use the steady-state composite of the storm simulations, which the hail growth trajectory model is run on; this way we can strip the problem to a simpler form and examine the effect of buoyancy and basic storm characteristics without the complexity of changing storm morphologies and structures. The parcels are then

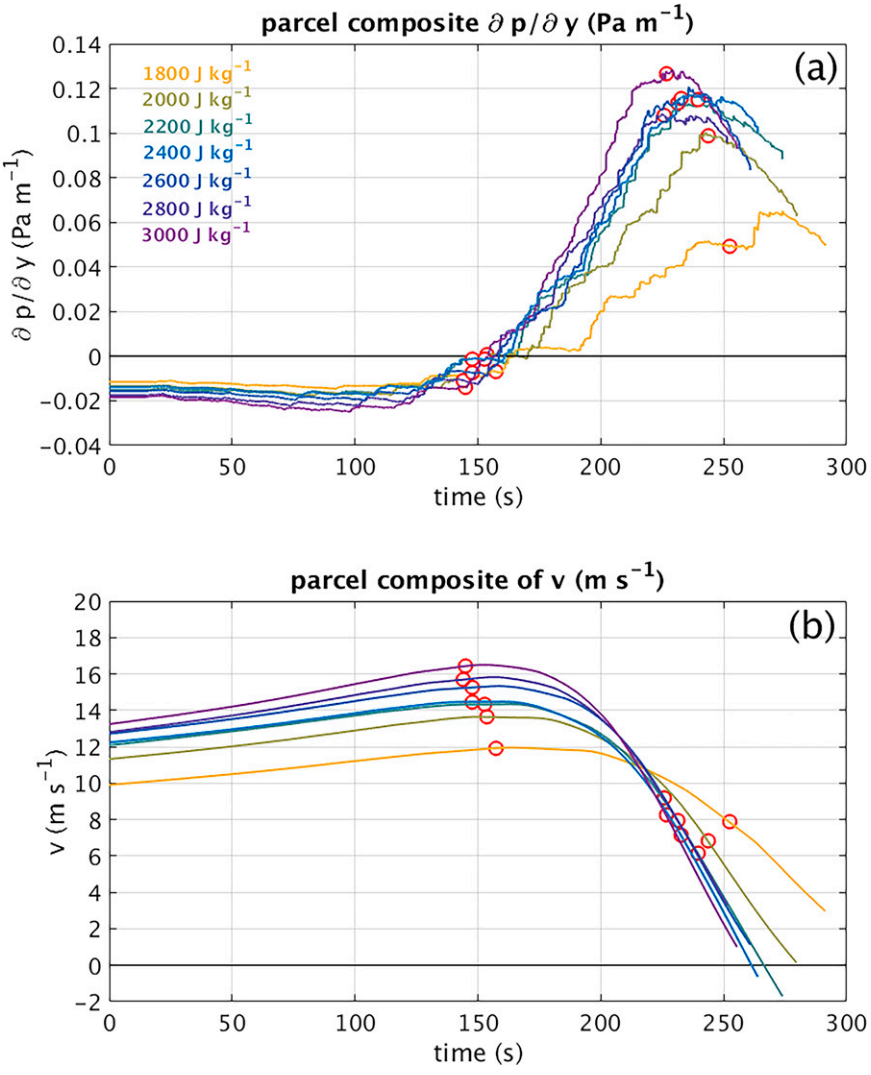

FIG. 13. Time series of (a) air parcel composite meridional pressure gradient (negative values imply a northward-pointing pressure gradient acceleration), and (b) v-wind speed component. The red circles on each line indicate the times when the parcel enters and exits the hail growth region. Each line represents a different CAPE value, colored according to the legend in (a). Increasing CAPE values correspond to cooler colors.

advected through the storm updraft using a simplified version of the Navier–Stokes equations, where only gravity and pressure gradient forces are considered:

$$\frac{D\mathbf{v}}{Dt} = -\frac{\nabla P}{\rho} - g\hat{\mathbf{k}}, \tag{3}$$

where D/Dt is the total derivative, $\mathbf{v}$ is the velocity vector, P is pressure, ρ is the air density, g is gravity, and $\hat{\mathbf{k}}$ is the vertical unit vector. The 15 parcels for each CAPE value are averaged, and the resulting composite meridional pressure gradient acceleration and parcel $v > 0$ speed are shown in Fig. 13. Inflow air parcels reach the negative pressure perturbation center early in their trajectory (Fig. 13a), typically even before they enter the optimal hail growth region aloft, owing to the large inflow speed and thus large initial northward momentum. Therefore, if the storm pressure field remains relatively unvaried[2] change in air parcels' speed largely depends on the time they ascend in the updraft after passing the pressure perturbation minimum. Because storms in environments with

[2] Storms in environments with greater CAPE tend to produce larger-magnitude pressure perturbations (e.g., Morrison 2016a,b; Peters et al. 2020a), so parcels in these simulations experience both greater accelerations and decelerations of their $v > 0$ speed (Fig. 13a); however, the shorter residence time during ascent in stronger updrafts seems to be the most important contributor to these results.

larger CAPE have stronger updrafts, air parcels ascend and eventually leave the hail growth region more rapidly (Fig. 13b), resulting in less time experiencing an adverse horizontal pressure gradient and thus less deceleration of their northward motion. Therefore, these faster-ascending parcels retain a greater portion of their horizontal inflow speed (Fig. 14).

With the preceding analysis, we refute the notion that larger CAPE generally promotes longer residence time for hailstones and, thus, larger hail. Now we examine the other important ingredient for hail growth–the supply of supercooled liquid water. According to parcel theory, a buoyant air parcel rises dry adiabatically until reaching saturation. The saturated air parcel then undergoes reversible adiabatic or pseudoadiabatic ascent (e.g., see Markowski and Richardson 2010; Murdzek et al. 2021). If the initial temperature and pressure at the lifting condensation level (LCL) are held constant, the liquid water a parcel produces (neglecting entrainment) should be approximately independent of the ambient environment on its rising path, including CAPE.[3] In other words, the vapor in excess of the equilibrium value at each level, given by the moist adiabat, is condensed out into liquid, regardless of CAPE.[4] And, if the initial thermodynamic condition and trajectory of an air parcel remain unchanged, it should produce the same amount of liquid water. Therefore, one could expect the LWC in the updraft to be greater for larger-CAPE cases only if the LCL temperature or pressure are significantly different compared to the smaller-CAPE cases. However, all RH profiles and mixed-layer temperature profiles are identical in our idealized simulations, leading to identical LCL temperatures and pressures for all cases. The temperature above the mixed layer is only *slightly* lower (about 2 K at 3 km AGL, yielding a difference of around 2 hPa in equilibrium vapor pressure) for the largest-CAPE case compared to the smallest one. Therefore, considering an idealized updraft only composed of air rising from the lowest levels, without entrainment of air from higher altitudes, we would expect similar LWC in updrafts for all CAPE values with only minor variance.

According to the bulk LWC within the 4–8-km updraft region (Fig. 5), however, an optimal range of CAPE values between 2000 and 2400 J kg^{-1} produces updrafts with greater median LWC values, pointing to differences in parcel origins. This relationship also holds true when accounting for only the LWC values experienced by hailstones along their trajectories (Fig. 15). According to the base-state thermodynamic profiles, air from the lowest altitudes can supply more moisture to the hail growth region because low-level parcels have greater vapor mixing ratios (i.e., more vapor content available to condense into liquid). Considering the discussion above, we hypothesize that updrafts composed of more air originating from the lowest levels would have larger LWC.

To evaluate this hypothesis, as a proxy of air parcels, we place passive tracers at low levels in the CM1 simulations and track their concentration at higher levels as they are ingested into the storm, along with entrained air. We launch tracers at

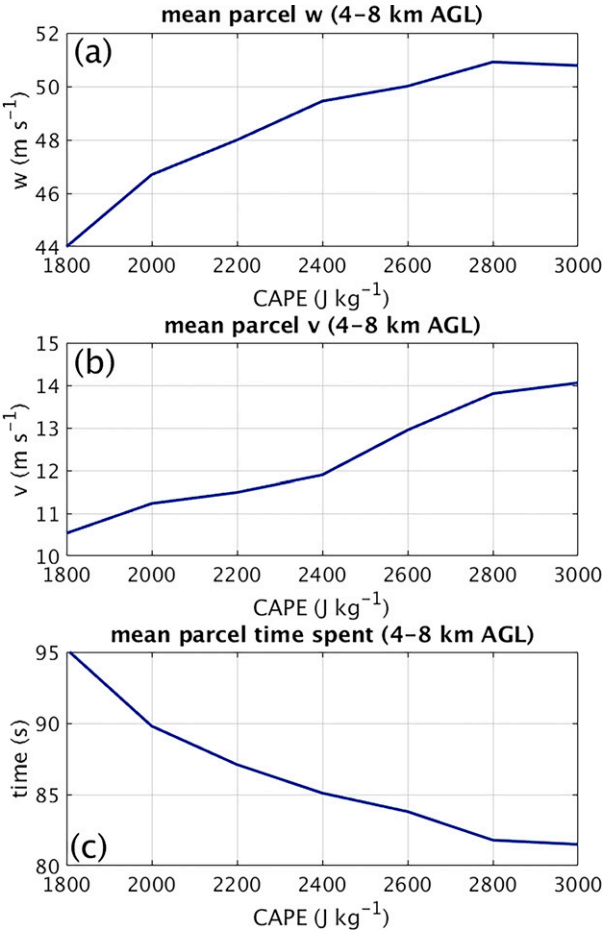

FIG. 14. Results of the parcel experiment calculations showing the relationships between CAPE and (a) mean vertical velocity w, (b) mean parcel v-wind component, and (c) mean parcel residence time within the hail growth zone.

17 different levels of our simulated storms at 1 kg kg^{-1} initial concentration: below 500 m AGL, from 500 to 1000 m AGL, from 1000 to 1500 m AGL, and so on until 7500–8000 m AGL, and, last, above 8000 m AGL. Similar to our prior analyses, we composite their concentrations for the second simulated hour with the domain shifted to be centered on the midlevel updraft maximum. Figure 16 presents the tracer fraction based on their source level and sampling level. For all CAPE values, the 4–8-km updraft region contains large amounts of air from the inflow layer (≲3 km AGL). The percentage of inflow-layer air ingested into the updraft seems to increase with CAPE, except perhaps for the CAPE = 3000 J

[3] In fact, parcel buoyancy could potentially affect its LWC (Romps 2015; Peters and Chavas 2021). For an adiabatically lifted parcel, moist static energy (MSE) minus CAPE is conserved, which could possibly alter its LWC and temperature.

[4] This assumes air parcels contain a sufficient number of aerosol to produce droplets and thus the parcels are limited only by supersaturation production (e.g., Lebo et al. 2012).

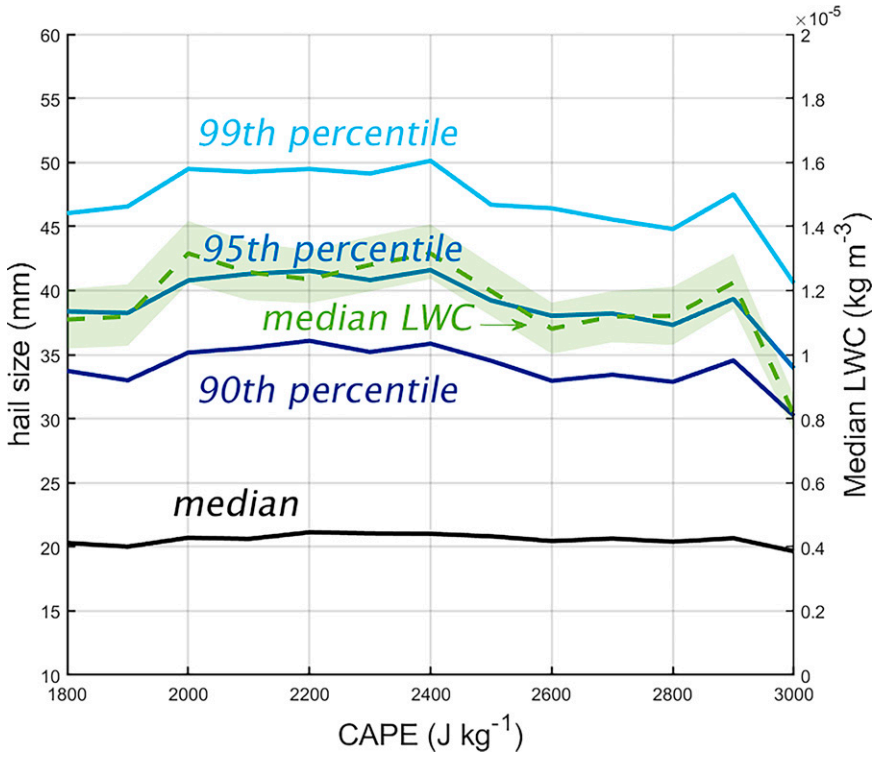

FIG. 15. As in Fig. 7, but the for median LWC experienced by hailstones along their trajectories (shown as a dashed green line, corresponding to the right ordinate axis) The shaded band around the median LWC line indicates the 95% confidence interval about the median values.

kg^{-1} case. Also evident in each case is air originating from higher altitudes: this implies that environmental air is entrained into the updraft (Nowotarski et al. 2020), where the initial environments are drier (cf. Fig. 1), meaning they contribute to decreased LWC.

Figure 17 demonstrates the percentages of tracers originating from the lowest 3 km AGL (i.e., the expected inflow layer) among all the tracers (red line) and the median LWC trend (blue line), both in the 20 m s^{-1} updraft within the hail growth region, as a function of CAPE. To facilitate comparison, the tracer percentage and LWC values have been normalized to their z score [$z = (x - \bar{x})/S$, where x is the raw data value, $\bar{x}$ is the sample mean, and S is the standard deviation]. A strong positive correlation ($\rho = 0.948$) is evident, suggesting that the percentage of moist inflow air ingested into the storm plays a role in the LWC within the storm's updraft. The remainder of air parcels composing the updraft in the hail growth region must have originated from above the inflow layer—i.e., they are entrained or ingested into the updraft from the drier free troposphere.

Peters et al. (2020b) suggest that the *fractional* entrainment of the storm updraft may decrease with CAPE due to its broadening area (McCaul and Weisman 2001; Kirkpatrick et al. 2011; Markowski and Richardson 2010; Peters et al. 2019) and increased updraft mass flux, even if the *total* amount of entrained mass increases due to the expansion of the updraft's boundary and increased horizontal speed of air that is entrained into the updraft (Morrison et al. 2020). This would mean that the remaining fraction of air in the updraft (i.e., that from the low-level inflow) increases with CAPE; our results contradict this expectation.

A reason behind the decrease in low-level air percentage for high CAPE values, and thus the non-monotonic LWC–CAPE relationship may lie in the storms' updraft morphology. By taking horizontal cross sections within the hail growth region at 5.375 km AGL and plotting the tracer concentrations from each source layer, we observe that the high-concentration centers for tracers from each origin level do not occupy the entire updraft area, nor do they substantially overlap (Fig. 18). The 20 m s^{-1} updraft area can be seen expanding as CAPE increases, whereas the locations and sizes of each tracer concentration maximum (representing where at this altitude has the most air originating from a given source level) remain mostly unchanged. Based on the shape and size of the updraft, as well as its collocation with the tracer concentration maxima, we hypothesize that the updraft area simultaneously "gobbles up" more lower-level air as well as higher-level entrained air as it expands, thus resulting in an optimal range of CAPE values when the ratios between the low-level and upper-level tracer concentrations is the greatest.

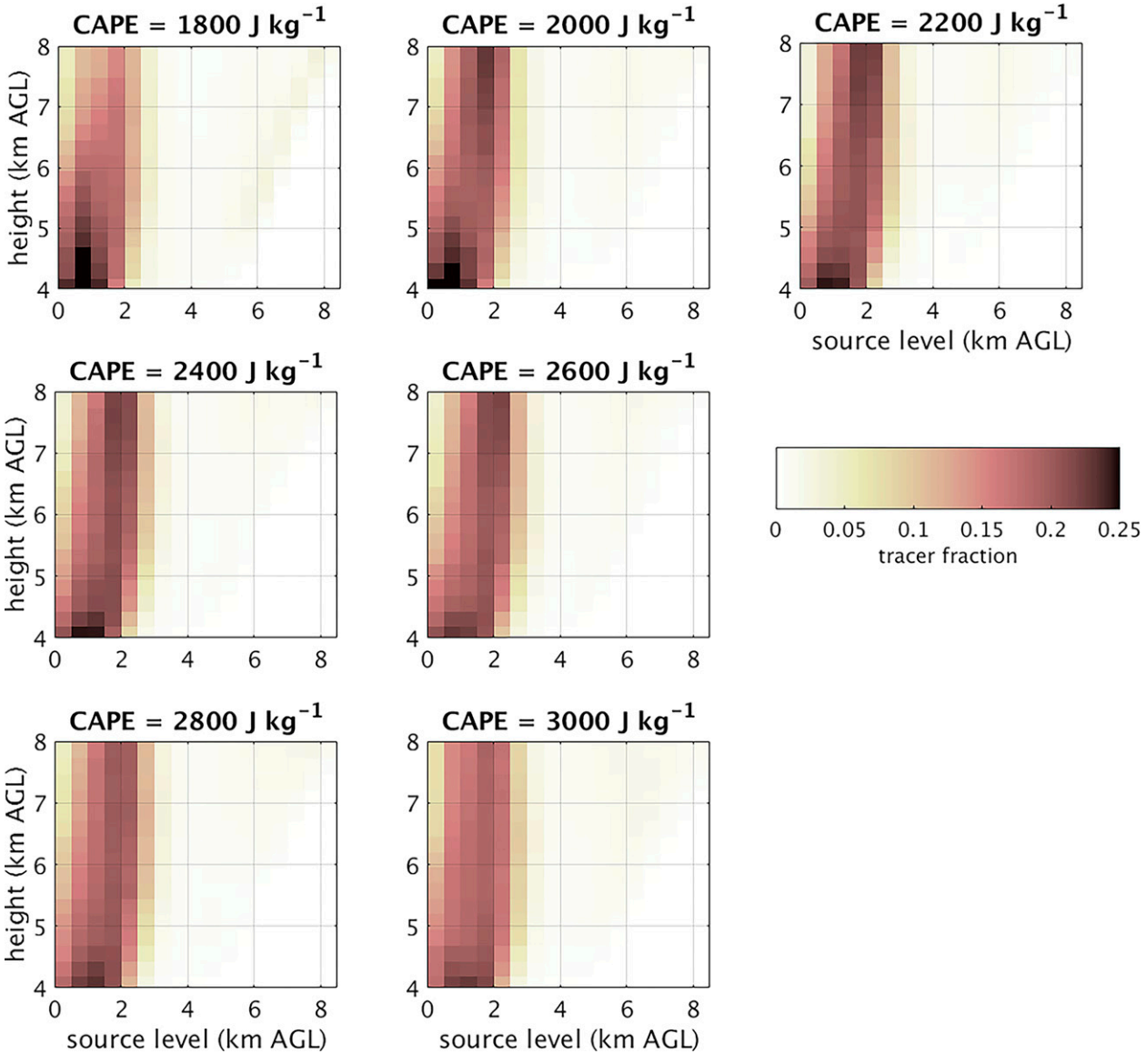

FIG. 16. Each panel shows the fraction of passive tracers at a given altitude (ordinate axis) as a function of the tracer source height (abscissa axis) for different CAPE simulations. The tracer fraction is shaded according to the outset color bar.

Figure 18 also shows that, at a given horizontal level aloft, air originating from different low-level altitudes tends to be concentrated in disparate locations in and around the updraft. To examine the cause of such clusterings, we launch a 30 × 30 × 3 km^3 cube of air parcels in CM1 within the 0–3 km AGL southeast inflow corner of the domain. The neighboring parcels are 500 m apart horizontally and 250 m apart vertically. Parcels begin being advected by the storm-relative winds through the domain at 1-h simulated time until the end of each 2-h simulation. Parcels from different originating layers start to diverge at the beginning of their advection: lower-level parcels move toward the west-northwest while higher-level parcels advect north-northwestward. Such differences in their early moments and thus early displacements lead to larger variations in their final trajectories, thus putting these parcels into clusters based on their respective initial altitudes (Fig. 19). A similar parcel sorting mechanism is discussed in Dahl (2017) (see their Fig. 10).

According to Holton and Hakim (2013), Davies-Jones (2015), and Dahl (2017), a Lagrangian surface (defined by the latter author as "the common height of parcels at an arbitrary reference time t_0") will exhibit a bulge downstream (in the storm-relative sense) of the maximum vertical velocity, and thereby downstream of the updraft. Because of hodograph curvature and the resulting change in storm-relative winds at different levels, this bulge/displacement will rotate around the

updraft for parcels originating at different initial heights. As a result, parcels from certain altitudes within the inflow layer will have a better chance of rising along the favorable hail path than others. As such, the water vapor content of these layers would affect hail growth the most. The heights of these layers are, in turn, influenced by the hodograph itself. For example, for the quarter-circle hodograph used in our simulations, the low-level storm-relative wind direction has a strong westward component and relatively weaker northward component; thus, parcels originating at low levels should be displaced west of the updraft maximum aloft (i.e., away from the favorable pathway for hailstone growth, see Fig. 3). In contrast, parcels originating at greater altitudes, where storm-relative winds have an eastward component, will find themselves displaced to the east of the midlevel updraft maximum (i.e., close to the favorable pathway for hailstone growth). For u31_z7, air from 1.5 to 3 km AGL concentrates more on the eastern side of the updraft, thus potentially influencing hail growth the most.

There are immediate forecasting implications based on this examination: instead of focusing on the low-level moisture conditions (e.g., surface or 100-hPa mean layer) air, a more relevant layer may be the one in which parcels found in the favorable hail trajectory region originate. In our simulations, for example, the majority of air located in the eastern half of the mesocyclone originates from the 1.5–3 km AGL layer, suggesting that the moisture conditions at these altitudes may could be important for modulating the LWC available in the hail growth region. *Thus, we propose that better forecasting of the hail threat may involve pairing the storm-relative wind profile and environmental moisture profile.* No doubt, this makes it challenging compared to traditional metrics.

Using the results from KL20, we can compare the sensitivity of hail size to changes in CAPE and changes in 0–6-km wind shear. For the u31z7 cases, when CAPE increases by 33.33% below the "optimal" CAPE value (from 1800 to 2400 J kg^{-1}, where hail size and CAPE are positively correlated), the amount of hailstones in the 30-, 40-, and 50-mm size bins increase by 79.72%, 137.50%, and 428.57%, respectively. In KL20, when the 0–6-km wind shear increases by 38.89% from 36 to 50 m s^{-1}, the amount of 30-, 40-, and 50-mm hailstones increases by 129.26%, 247.96%, and 516.06%, respectively. Thus, for comparable changes in shear and CAPE (as CAPE increases to the optimal values in our chosen range), the amount of larger hail increases in a commensurate manner.

b. *Deep-layer shear (z7) experiments*

In the previous subsection, we examined how variations in CAPE affect hail size, but held the wind profile constant. In addition to thermodynamic conditions, vertical wind shear also plays a crucial role in modulating hail production by affecting the morphology of the storm updraft and storm wind field (e.g., Weisman and Klemp 1982; Brooks et al. 1994; Weisman and Rotunno 2000). DK17 have demonstrated that a strong zonal component to the deep-layer shear vector could potentially enhance hail production in simulated supercell storms by elongating the storm updraft in the direction of the shear

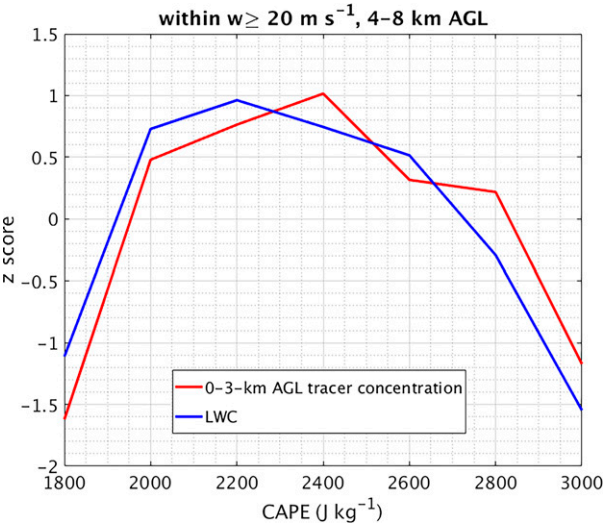

FIG. 17. Red line indicates tracer concentration originating from <3 km AGL, and the blue line is the LWC within the $w \geq 20$ m s^{-1} updraft in the hail growth region, as a function of CAPE for the u31_z7 simulations. Both have been normalized by their z score to facilitate comparison. For the actual values, see the supplemental material.

vector, thus increasing the volume in which hailstones can collect mass and increase in size. These results were supported by KL20, who found that hailstone residence time increases with increasing zonal deep-layer shear. However, these studies all used fixed thermodynamic profiles; as such, it is an open question how variations in CAPE *and* shear modulate hail growth. We address this question in this section by varying CAPE (as before) for three different amounts of deep-layer shear by using u_{max} = 25, 31, and 36 m s^{-1}.

Figure 20 (left column) shows hail size metrics as a function of CAPE for these three shear values. All three sets of experiments demonstrate a similar hail size–CAPE relationship, where an optimal, larger-hail-producing state exists for intermediate CAPE values. This potentially results from the non-monotonic relationships between residence time and CAPE, and updraft LWC and CAPE (Fig. 20, left column). Further, this relation appears to become more pronounced with increasing shear. Just as we observed in the u31_z7 experiments, there is also a significant positive correlation between ATS ratio and residence time (not shown).

Despite the similarities in the observed hail size–CAPE relationship for each shear case, differences do exist between the weak (u_{max} = 25 m s^{-1}) and strong (u_{max} = 36 m s^{-1}) shear cases. First, storms with the same CAPE have a larger updraft area as deep-layer shear increases (Fig. 21a), which can be explained by the hypothesis in Peters et al. (2019) that updraft area is strongly influenced by the low-level inflow, and subsequently by the low-level storm-relative wind. The increase in low-level storm-relative wind also leads to greater in-storm horizontal wind speed; however, because we only vary the westerly deep-layer wind shear, the southerly storm-relative wind (the leading contributor to the southerly in-updraft wind), does not change as drastically (Fig.

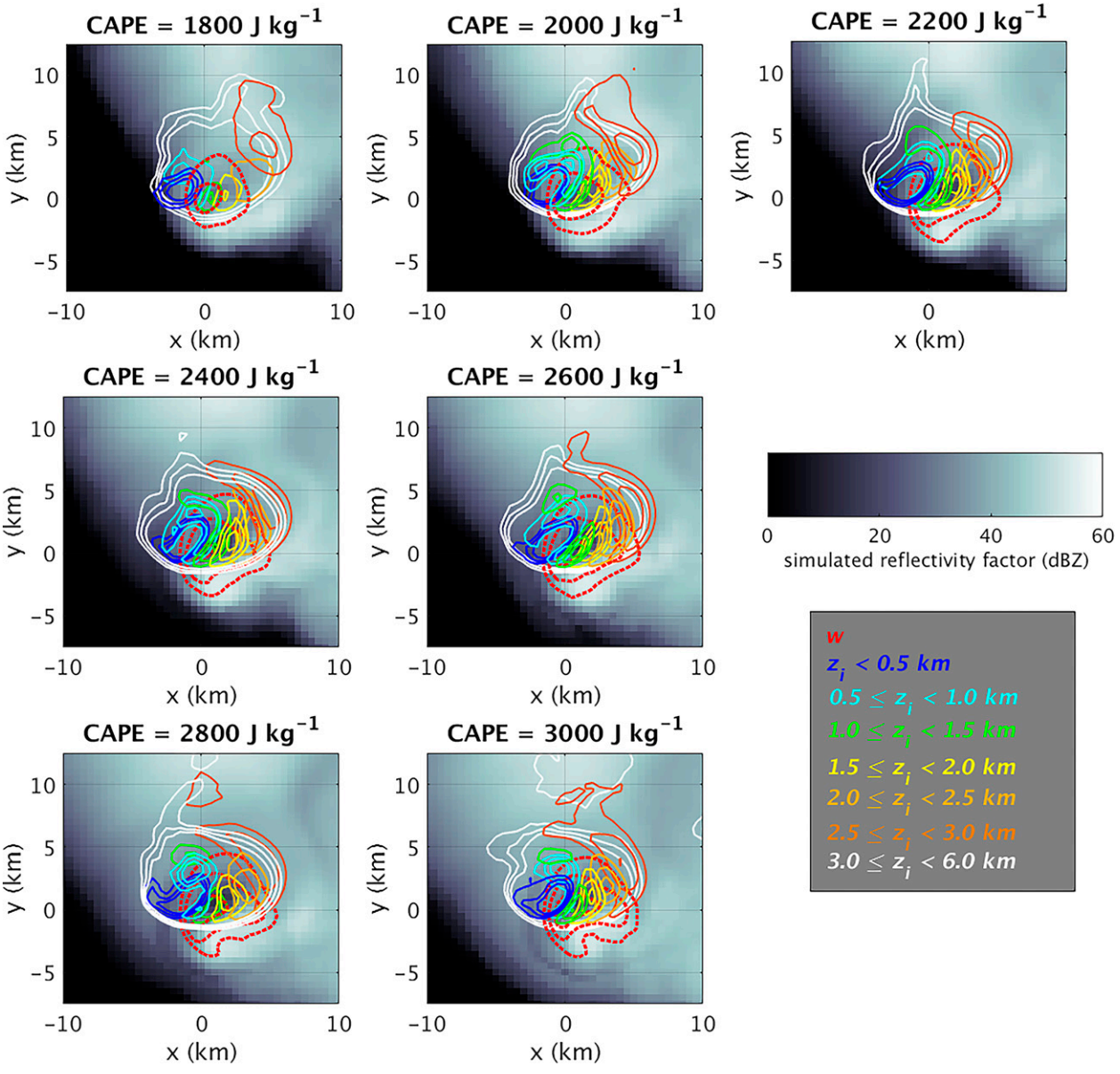

FIG. 18. Horizontal cross sections at 5.375 km AGL with shading indicating simulated radar reflectivity (dBZ, according to scale). Tracer mixing ratio values of 0.3, 0.4, and 0.5 kg kg^{-1} are contoured and colored by initial height, with those originating from below 0.5 km AGL shown in dark blue, 0.5–1.0 km AGL in cyan, 1.0–1.5 km AGL in green, 1.5–2.5 km AGL in yellow, 2.0–2.5 km AGL in marigold, 2.5–3.0 km AGL in orange, and 3.0–6.0 km AGL in white. The red dashed lines are the updraft 20, 30, and 40 m s^{-1} contours.

21b). As a result, the ATS ratio increases with deep-layer shear (Fig. 21c), leading to greater hailstone residence times.

Repeating the tracer experiment from the previous subsection, we evaluate the relationship between the low-level air concentration and the updraft LWC median in both sets of experiments. For u36_z7 (Fig. 22a), the correlation is strong and significant ($\rho = 0.866$, p value = 0.012). However, for u25_z7 (Fig. 22b), the low-level air concentration does not relate well with the LWC medians. One possible reason is the weaker updrafts. With weaker shear, the storm updraft is smaller and weaker if CAPE is relatively low (≤2000 J kg^{-1}), and the ingestion of tracers is slower. At the beginning of the second simulated hour (the starting time step of our storm composite), although the amount of low-level tracers in all other cases exhibits steady decrease as tracers are being advected upward and out of the hail growth region, the low-level tracers in the u25_z7_1600, u25_z7_1800, and u25_z7_2000 updrafts are still increasing or fluctuating, resulting in greater amounts. Because low-level tracer concentration is merely a proxy

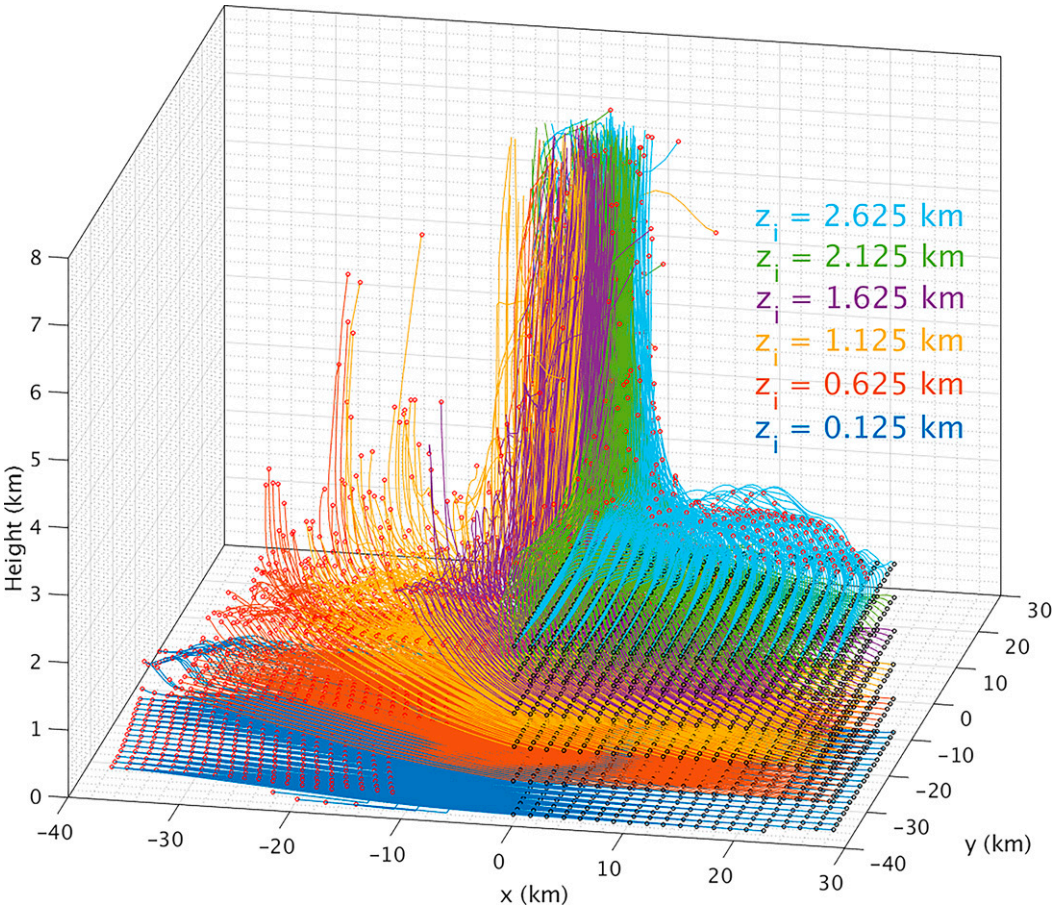

FIG. 19. Three-dimensional view of parcels initialized in the inflow (southeastern) portion of the domain. The initial parcel heights are indicated by different colors, according to the inset legend. Parcel initial locations are black circle markers, and final locations are red circle markers. Note the west-to-east change in locations and trajectory directions for increasing initial heights, reflecting the hodograph.

for, and *not* an exact representative of, the low-level air concentration, using the low-level tracer percentage for weak-shear, low-CAPE cases results in an overestimation of the fraction of low-level air within the updraft.

The 5.375 km AGL horizontal cross sections for all three shear cases (Fig. 23) show similar clustering patterns of different-initial-altitude tracer concentration maxima, suggesting that there is more lower-level inflow air in the western side of the updraft, and more higher-level inflow air in the eastern side. As expected owing to the variation in low-level storm-relative winds for these three shear cases, the west-to-east spread of the different tracer concentration maxima increases with increased zonal deep-layer shear. For example, the separation of the <0.5 and 2.5–3.0 km AGL tracer concentration maxima increases from ~5 km for u25_z7_2400 to ~6.5 km for u31_z7_2400, to ~7.8 km for the u36_z7_2400 case. These results suggest that the horizontal placement of different-initial-altitude inflow air changes with shear, meaning that the importance of low-level layer inflow air originating from different altitudes may vary according to a storm's hodograph.

c. *Buoyancy profile experiments*

Other characteristics of the buoyancy profile, besides CAPE, can also modulate hail production by influencing storm features (McCaul and Cohen 2002; McCaul et al. 2005). For example, it is commonly thought that larger midlevel lapse rates could be favorable for increased hail size (e.g., Johnson and Sugden 2014; Tang et al. 2019, see also the Storm Prediction Center's "significant hail parameter"). Lapse rate is directly linked to the overall CAPE value and the vertical distribution of buoyancy. By keeping the same CAPE and wind profile, we can vary the vertical buoyancy distribution by adjusting the level of maximum buoyancy (Z_B). Figure 24 shows lapse rate profiles for u31_1800 and u31_3000, where Z_B varies between 6 and 8 km AGL. Although the lapse rate differences resulting from Z_B variations are less significant than those resulting from CAPE variations, we expect larger midlevel lapse rates for larger Z_B, where buoyancy is concentrated at

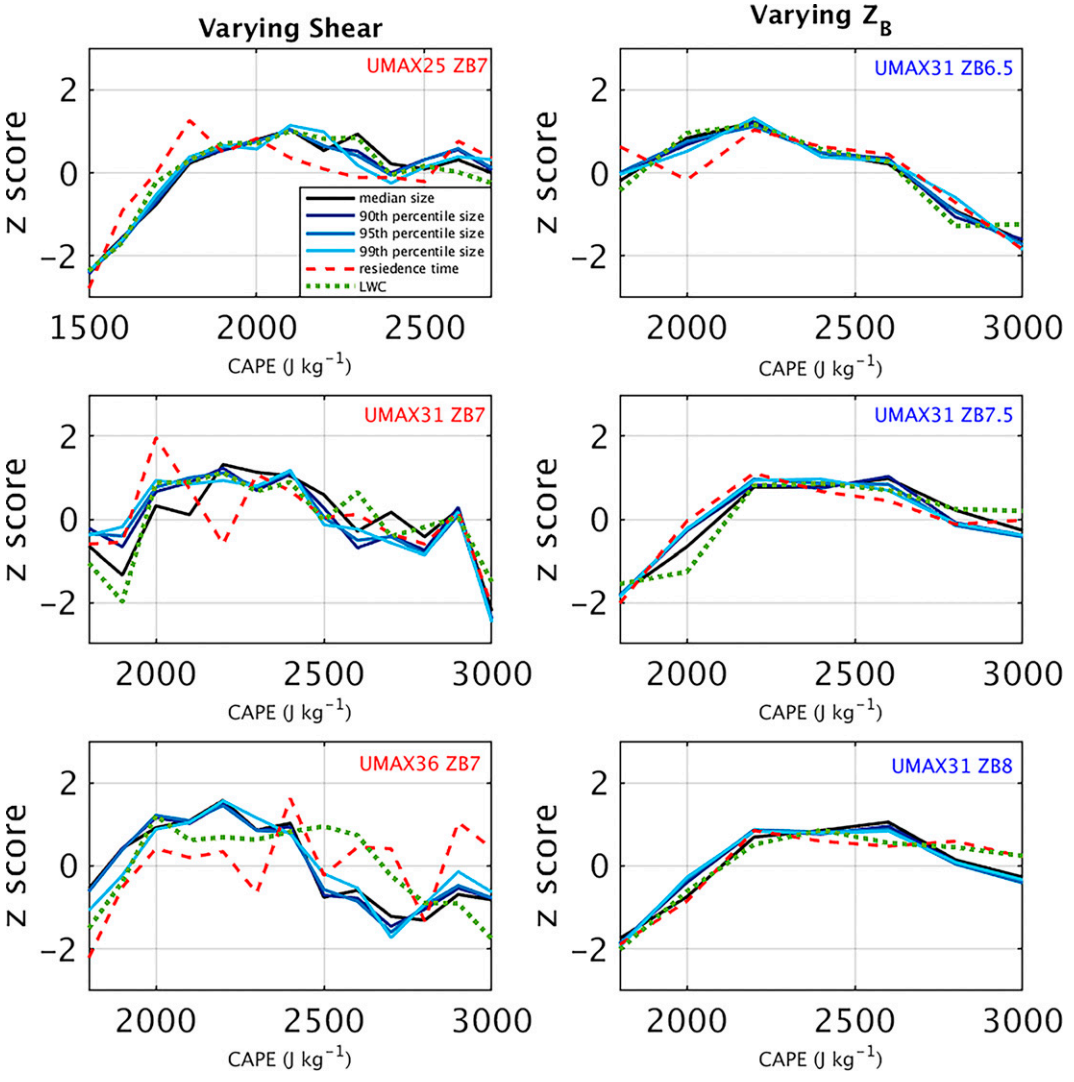

FIG. 20. As in Fig. 7, but for different sounding configurations with varying deep-layer shear and Z_B (indicated by colored text at the upper-right corner of each panel). (left) Shear experiments with varying u_{max} (m s^{-1}) and (right) buoyancy distribution experiments with varying Z_B (km AGL). All values are normalized to their z score to facilitate comparison; see the supplemental material for the actual values.

higher altitudes. As Z_B increases from 6.5 to 8.0 km AGL, we observe a shift in optimal CAPE values for storms that produce larger hail from 2000–2400 to 2200–2600 J kg^{-1} (Fig. 20, right column). Additionally, the amount of large hail as well as the 95th and 99th percentile hail sizes for cases larger CAPE (≤2200 J kg^{-1}) increase with Z_B (not shown), suggesting that, with the same amount of higher CAPE, supercell storms with less buoyancy at the lower levels (i.e., a less "bottom-heavy" buoyancy profile) produce larger hail.

The changes in hail production arise because a larger Z_B is associated with smaller horizontal wind speed in the hail growth region while maintaining a similar mean updraft area, at least for CAPE ≥ 2200 J kg^{-1} (Figs. 25a,b). This is consistent with our discussion in section 3a that the in-updraft southerly wind speed is positively related to inflow speed as well as updraft speed, both of which decrease with increasing Z_B, whereas updraft area is only strongly positively correlated to the inflow speed (Peters et al. 2019). The ATS ratio (Fig. 25c) demonstrates the competition between updraft area and horizontal flow, and potentially the increase the peak residence time for supercells in environments with larger Z_B.

4. Conclusions

The relationship between CAPE and hail size in simulated supercell storms is examined in this paper, with particular focus on factors influencing hailstones' residence time in the mixed-phase region of the updraft. The notion

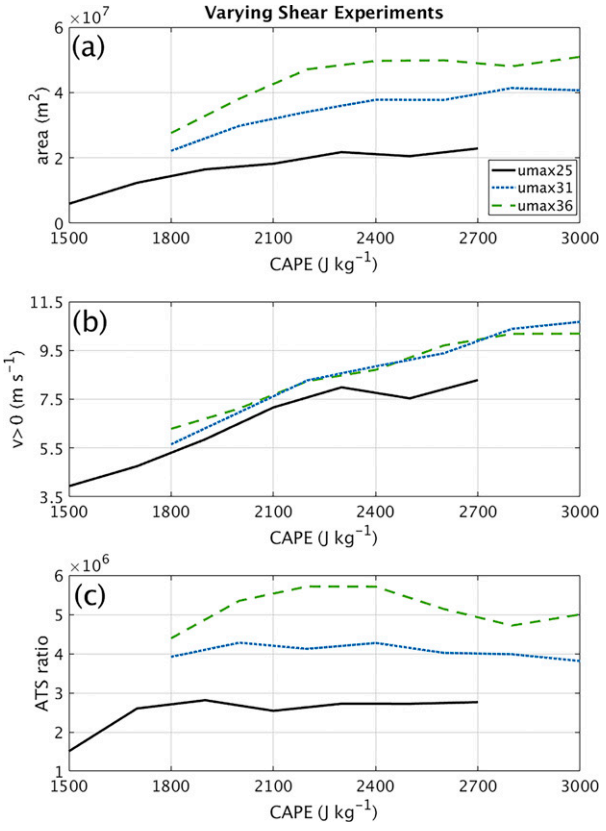

FIG. 21. Change in (a) mean updraft area, (b) mean southerly ($v > 0$) wind speed, and (c) ATS ratio, all sampled within the 20 m s^{-1} updraft between 4 and 8 km AGL, as a function of CAPE for the varying shear experiments, according to the legend.

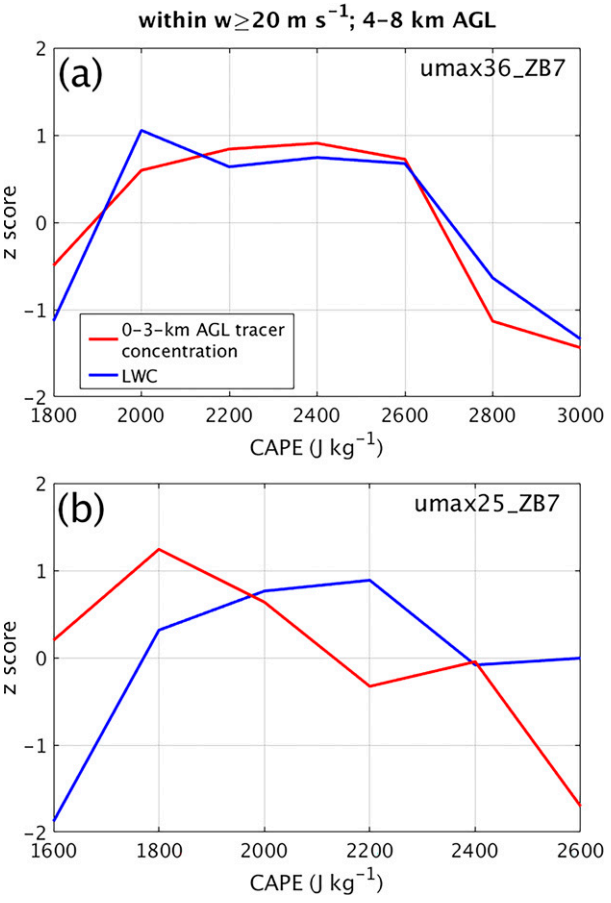

FIG. 22. As in Fig. 17, but for (a) u36_z7 and (b) u25_z7. The values are normalized to their z score to facilitate comparison; see the supplemental material for the actual values.

that storms with greater CAPE produce larger hail apparently is widespread in the forecasting community. Conventional wisdom suggests that, because storms with larger CAPE have stronger updrafts, they thereby have the ability to "support" hailstones for a longer period of time.

However, through a series of numerical simulations coupled with our hailstone growth trajectory model calculations, we have found that residence time (and thus hail size) *does not increase* monotonically with CAPE, but instead maximizes for an intermediate range of "optimal" CAPE values within our specific shear-CAPE parameter space, representing high-CAPE supercell storms (e.g., Púčik et al. 2015; Blair et al. 2017; Taszarek et al. 2020). These results are related to increases in updraft width and changes in horizontal flow within the updraft as CAPE increases. The reasons for updraft expansion with increased CAPE are still an active topic of research in which theoretical approaches and simulation results sometimes conflict (e.g., Peters et al. 2019). Using the conceptual framework from Peters et al. (2019), however, we hypothesize that, because increased CAPE leads to storm motion farther off the hodograph, low-level storm-relative wind speeds are increased, resulting in wider updrafts. On the other hand, the larger southerly wind within the updraft with increased CAPE is a result of larger inflow speed, as well as the interaction between rising parcels and the storms' pressure perturbation fields. In particular, faster-ascending parcels in stronger updrafts (larger-CAPE environments) spend *less time* facing an adverse horizontal perturbation pressure gradient force, thereby retaining greater northbound speeds than their slower-ascending counterparts in smaller-CAPE environments. Another important "ingredient" for hail growth—LWC within the updraft—also exhibits a non-monotonic relationship with CAPE owing to changes in the horizontal distribution (across the midlevel updraft) of moist air rising from different altitudes within the inflow layer, as well as changes to the amount of entrained dry free tropospheric air.

With these findings, it is unsurprising that neither hail size nor the amount of severe hail increases monotonically with CAPE in our simulations; rather, hail size metrics maximize for an optimal intermediate range of CAPE values in the range chosen for this study, similar to hailstones' residence time within the optimal hail growth region (Fig. 20). Superposed on these

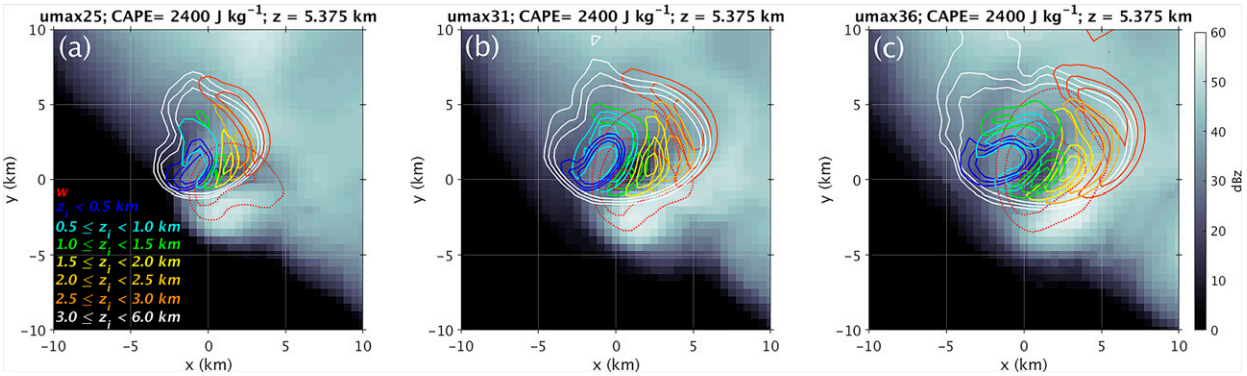

FIG. 23. As in Fig. 18, but for the varying shear simulations (a) u25_z7_2400, (b) u31_z7_2400, and (c) u36_z7_2400.

results is overall increase in hail size for larger zonal deep-layer shear, similar to DK17 and KL20. Further examinations in adjusting the vertical distribution of buoyancy reveal that the optimal CAPE range for hail production can vary even with a fixed amount of CAPE, owing to the consequent variations in the updraft's flow field.

Is there observational evidence to support these findings? Brooks (2013, their Fig. 1) shows a relationship between theoretical maximum vertical velocity (calculated from CAPE) and the probability of hailstones > 50 mm that exhibits a similar trend to the CAPE–hail size relationship found in our study, where the probability increases with maximum vertical velocity to a certain point before decreasing as maximum vertical velocity increases further. However, the optimal CAPE range for significantly severe hail presented by (Brooks 2013) is below the chosen CAPE range tested here. Figure 9a in Taszarek et al. (2020) also shows a similar pattern, but only for a limited parameter space where 0–6-km wind shear is between 20 and 30 m s^{-1}, where the probabilities of storms producing hailstones > 20 mm increase with MLCAPE until about 4000 J kg^{-1}, then decrease as MLCAPE increases further until it reaches a second peak at about 5000 J kg^{-1} in relatively low shear space (near 15 m s^{-1}). The same trend is also seen in their Fig. 9b, but for hailstones > 50 mm in storms with 0–6-km wind shear between 15 and 25 m s^{-1}.

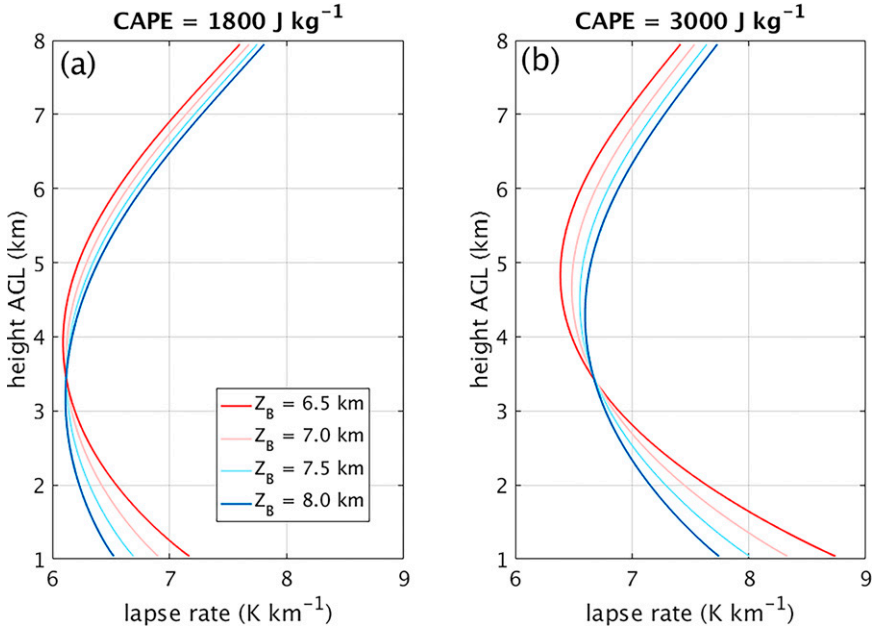

FIG. 24. Vertical profiles of temperature lapse rate (K km^{-1}) for the (a) u31_1800 and (b) u31_3000 simulations. Each color represents a different Z_B, according to the legend. Cooler colors indicate greater Z_B.

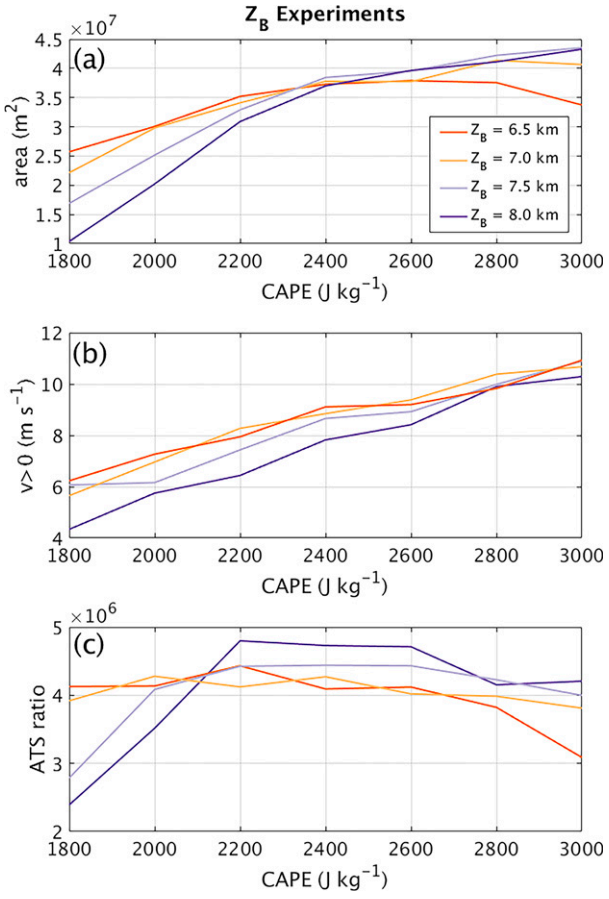

FIG. 25. (a)–(c) As in Fig. 21, but for u31 experiments with varying buoyancy profiles. Each color represents a different Z_B, indicated by the legend in (a). Cooler colors indicate increasing Z_B.

With our analysis herein, we cast doubt on the notion that larger CAPE generally would promote longer residence time for hailstones and, thus, larger hail. In light of our results, it is perhaps unsurprising that past climatologies have not found CAPE to be a useful discriminator of hail size classes (Craven et al. 2004; Johnson and Sugden 2014; Púčik et al. 2015; Blair et al. 2017). Given that hailstones are typically advected across the updraft during their growth (Nelson 1983; Ziegler et al. 1983; Foote 1984), it is logical for the horizontal wind field, as well as the morphology of the updraft and mesocyclone, to be important for controlling residence time, instead of a simple linear relationship to CAPE.

The determining factor of the southerly wind component is specific to our hodograph, and thereby storm morphology. In forecast applications, the most significant wind component might change based on the supercells' environmental wind fields, depending on the shear direction, hemisphere, etc. However, the general idea remains unchanged that the storm's updraft area and horizontal wind field, instead of CAPE, are the main factors in influencing hailstones' residence time and thus the final hail size.

Acknowledgments. Support for the first and second authors of this research comes from NSF Grant AGS-1855063. The second author is also supported by NSF Grants AGS-1661679 and an award from the Insurance Institute for Business and Home Safety. We thank the National Center for Atmospheric Research for providing and maintaining the Cheyenne supercomputing facility, and George Bryan for building and maintaining the CM1 code. We also acknowledge useful conversations with John Peters (Naval Postgraduate School) and Hughbert Morrison (NCAR) on factors controlling updraft width, and for feedback and suggestions throughout the research from Rebecca Adams-Selin (AER), John Allen and Cameron Nixon (Central Michigan University), and Conrad Ziegler (NSSL). We also thank Kelly Lombardo (PSU), Shawn Murdzek (PSU), and Zachary Lebo (Univ. of Wyoming) for their assistance with the pressure perturbation calculations. We would also like to acknowledge high-performance computing support from Cheyenne (doi:10.5065/D6RX99HX) provided by NCAR's Computational and Information Systems Laboratory, sponsored by the National Science Foundation. Finally, we acknowledge the thorough and careful reviews from the anonymous reviewers that helped substantially improve the clarity of the paper.

Data availability statement. The source code for CM1 is freely available from NCAR. The code for creating input soundings and the soundings used here are available from the first author (and will be placed on PSU Data Commons when in final form). The hail trajectory code is available from the second author.

REFERENCES

Adams, J. C., 1999: MUDPACK: Multigrid software for elliptic partial differential equations. NCAR, accessed 8 June 2020, https://www2.cisl.ucar.edu/resources/legacy/mudpack.

Adams-Selin, R. D., and C. L. Ziegler, 2016: Forecasting hail using a one-dimensional hail growth model within WRF. *Mon. Wea. Rev.*, **144**, 4919–4939, https://doi.org/10.1175/MWR-D-16-0027.1.

——, A. J. Clark, C. J. Melick, S. R. Dembek, I. L. Jirak, and C. L. Ziegler, 2019: Evolution of WRF-HAILCAST during the 2014–16 NOAA/Hazardous Weather Testbed Spring Forecasting Experiments. *Wea. Forecasting*, **34**, 61–79, https://doi.org/10.1175/WAF-D-18-0024.1.

Allen, J. T., and M. K. Tippett, 2015: The characteristics of United States hail reports: 1955–2014. *Electron. J. Severe Storms Meteor.*, **10** (3), https://ejssm.org/archives/2015/vol-10-3-2015/.

Blair, S. F., D. R. Deroche, J. M. Boustead, J. W. Leighton, B. L. Barjenbruch, and W. P. Gargan, 2011: A radar-based assessment of the detectability of giant hail. *Electron. J. Severe Storms Meteor.*, **6** (7), https://ejssm.org/archives/2011/vol-6-7-2011/.

——, and Coauthors, 2017: High-resolution hail observations: Implications for NWS warning operations. *Wea. Forecasting*, **32**, 1101–1119, https://doi.org/10.1175/WAF-D-16-0203.1.

Brimelow, J. C., G. W. Reuter, and E. R. Poolman, 2002: Modeling maximum hail size in Alberta thunderstorms. *Wea.*

Forecasting, **17**, 1048–1062, https://doi.org/10.1175/1520-0434(2002)017<1048:MMHSIA>2.0.CO;2.

Brooks, H. E., 2013: Severe thunderstorms and climate change. *Atmos. Res.*, **123**, 129–138, https://doi.org/10.1016/j.atmosres.2012.04.002.

——, C. A. Doswell, and R. B. Wilhelmson, 1994: The role of midtropospheric winds in the evolution and maintenance of low-level mesocyclones. *Mon. Wea. Rev.*, **122**, 126–136, https://doi.org/10.1175/1520-0493(1994)122<0126:TROMWI>2.0.CO;2.

Browning, K. A., and G. B. Foote, 1976: Air-flow and hail growth in supercell storms and some implications for hail suppression. *Quart. J. Roy. Meteor. Soc.*, **102**, 499–533, https://doi.org/10.1002/qj.49710243303.

Bryan, G. H., and J. M. Fritsch, 2002: A benchmark simulation for moist nonhydrostatic numerical models. *Mon. Wea. Rev.*, **130**, 2917–2928, https://doi.org/10.1175/1520-0493(2002)130<2917:ABSFMN>2.0.CO;2.

Chisholm, A. J., and M. English, 1973: *Alberta Hailstorms. Meteor. Monogr.*, No. 36, Amer. Meteor. Soc., 98 pp.

Conway, J. W., and D. S. Zrnić, 1993: A study of embryo production and hail growth using dual-Doppler and multiparameter radars. *Mon. Wea. Rev.*, **121**, 2511–2528, https://doi.org/10.1175/1520-0493(1993)121<2511:ASOEPA>2.0.CO;2.

Craven, J. P., and H. E. Brooks, 2004: Baseline climatology of sounding derived parameters associated with deep moist convection. *Natl. Wea. Dig.*, **28**, 13–24, https://www.nssl.noaa.gov/users/brooks/public_html/papers/cravenbrooksnwa.pdf.

Dahl, J., 2017: Tilting of horizontal shear vorticity and the development of updraft rotation in supercell thunderstorms. *J. Atmos. Sci.*, **74**, 2997–3020, https://doi.org/10.1175/JAS-D-17-0091.1.

Davies-Jones, R. P., 2015: A review of supercell and tornado dynamics. *Atmos. Res.*, **158–159**, 274–291, https://doi.org/10.1016/j.atmosres.2014.04.007.

Dennis, E. J., and M. R. Kumjian, 2017: The impact of vertical wind shear on hail growth in simulated supercells. *J. Atmos. Sci.*, **74**, 641–663, https://doi.org/10.1175/JAS-D-16-0066.1.

Duda, J. D., and W. A. Gallus, 2010: Spring and summer Midwestern severe weather reports in supercells compared to other morphologies. *Wea. Forecasting*, **25**, 190–206, https://doi.org/10.1175/2009WAF2222338.1.

Edwards, R., and R. L. Thompson, 1998: Nationwide comparisons of hail size with WSR-88D vertically integrated liquid water and derived thermodynamic sounding data. *Wea. Forecasting*, **13**, 277–285, https://doi.org/10.1175/1520-0434(1998)013<0277:NCOHSW>2.0.CO;2.

English, M., 1973: Growth of large hail in the storm. *Alberta Hailstorms, Meteor. Monogr.*, No. 36, Amer. Meteor. Soc., 37–98.

Foote, G. B., 1984: A study of hail growth utilizing observed storm conditions. *J. Climate Appl. Meteor.*, **23**, 84–101, https://doi.org/10.1175/1520-0450(1984)023<0084:ASOHGU>2.0.CO;2.

Gagne, D. J., A. McGovern, S. E. Haupt, R. A. Sobash, J. K. Williams, and M. Xue, 2017: Storm-based probabilistic hail forecasting with machine learning applied to convection-allowing ensembles. *Wea. Forecasting*, **32**, 1819–1840, https://doi.org/10.1175/WAF-D-17-0010.1.

Grant, L. D., and S. C. van den Heever, 2014: Microphysical and dynamical characteristics of low-precipitation and classic supercells. *J. Atmos. Sci.*, **71**, 2604–2624, https://doi.org/10.1175/JAS-D-13-0261.1.

Groenemeijer, P. H., and A. van Delden, 2007: Sounding-derived parameters associated with large hail and tornadoes in the Netherlands. *Atmos. Res.*, **83**, 473–487, https://doi.org/10.1016/j.atmosres.2005.08.006.

Guan, Y., F. Zheng, P. Zhang, and C. Qin, 2015: Spatial and temporal changes of meteorological disasters in China during 1950–2013. *Nat. Hazards*, **75**, 2607–2623, https://doi.org/10.1007/s11069-014-1446-3.

Gunturi, P., and M. Tippett, 2017: Managing severe thunderstorm risk: Impact of ENSO on U.S. tornado and hail frequencies. WillisRe Tech. Rep., 5 pp., http://www.columbia.edu/~mkt14/files/WillisRe_Impact_of_ENSO_on_US_Tornado_and_Hail_frequencies_Final.pdf.

Hersbach, H., and Coauthors, 2020: The ERA5 global reanalysis. *Quart. J. Roy. Meteor. Soc.*, **146**, 1999–2049, https://doi.org/10.1002/qj.3803.

Heymsfield, A. J., 1983: Case-study of a hailstorm in Colorado. Part IV: Graupel and hail growth mechanisms deduced through particle trajectory calculations. *J. Atmos. Sci.*, **40**, 1482–1509, https://doi.org/10.1175/1520-0469(1983)040<1482:CSOAHI>2.0.CO;2.

——, A. R. Jameson, and H. W. Frank, 1980: Hail growth mechanisms in a Colorado hailstorm. Part II: Hail formation processes. *J. Atmos. Sci.*, **37**, 1779–1807, https://doi.org/10.1175/1520-0469(1980)037<1779:HGMIAC>2.0.CO;2.

——, M. Szakáll, A. Jost, I. Giammanco, and R. Wright, 2018: A comprehensive observational study of graupel and hail terminal velocity, mass flux, and kinetic energy. *J. Atmos. Sci.*, **75**, 3861–3885, https://doi.org/10.1175/JAS-D-18-0035.1.

Holton, J. R., and G. J. Hakim, 2013: *An Introduction to Dynamic Meteorology*. Academic Press, 552 pp.

Jewell, R., and J. Brimelow, 2009: Evaluation of Alberta hail growth model using severe hail proximity soundings from the United States. *Wea. Forecasting*, **24**, 1592–1609, https://doi.org/10.1175/2009WAF2222230.1.

Johnson, A. W., and K. E. Sugden, 2014: Evaluation of sounding-derived thermodynamic and wind-related parameters associated with large hail events. *Electron. J. Severe Storms Meteor.*, **9** (5), https://ejssm.org/archives/2014/vol-9-5-2014/.

Kahraman, A., S. Tilev-Tanriover, M. Kadioglu, D. M. Schultz, and P. M. Markowski, 2016: Severe hail climatology in Turkey. *Mon. Wea. Rev.*, **144**, 337–346, https://doi.org/10.1175/MWR-D-15-0337.1.

Kaltenböck, R., G. Diendorfer, and N. Dotzek, 2009: Evaluation of thunderstorm indices from ECMWF analyses, lightning data and severe storm reports. *Atmos. Res.*, **93**, 381–396, https://doi.org/10.1016/j.atmosres.2008.11.005.

Kennedy, P. C., and A. G. Detwiler, 2003: A case study of the origin of hail in a multicell thunderstorm using in situ aircraft and polarimetric radar data. *J. Appl. Meteor.*, **42**, 1679–1690, https://doi.org/10.1175/1520-0450(2003)042<1679:ACSOTO>2.0.CO;2.

Khvorostyanov, V. I., and J. A. Curry, 2002: Terminal velocities of droplets and crystals: Power laws with continuous parameters over the size spectrum. *J. Atmos. Sci.*, **59**, 1872–1884, https://doi.org/10.1175/1520-0469(2002)059<1872:TVODAC>2.0.CO;2.

Kirkpatrick, C., E. W. McCaul, and C. Cohen, 2011: Sensitivities of simulated convective storms to environmental CAPE. *Mon. Wea. Rev.*, **139**, 3514–3532, https://doi.org/10.1175/2011MWR3631.1.

Klemp, J. B., and R. Wilhelmson, 1978: The simulation of three-dimensional convective storm dynamics. *J. Atmos. Sci.*, **35**,

1070–1096, https://doi.org/10.1175/1520-0469(1978)035<1070:TSOTDC>2.0.CO;2.

Kumjian, M. R., and K. A. Lombardo, 2020: A hail growth trajectory model for exploring the environmental controls on hail size: Model physics and idealized tests. *J. Atmos. Sci.*, **77**, 2765–2791, https://doi.org/10.1175/JAS-D-20-0016.1.

——, ——, and S. Loeffler, 2021: The evolution of hail production in simulated supercell storms. *J. Atmos. Sci.*, **78**, 3417–3440, https://doi.org/10.1175/JAS-D-21-0034.1.

Kunz, M., U. Blahak, J. Handwerker, M. Schmidberger, H. J. Punge, S. Mohr, E. Fluck, and K. M. Bedka, 2018: The severe hailstorm in southwest Germany on 28 July 2013: Characteristics, impacts and meteorological conditions. *Quart. J. Roy. Meteor. Soc.*, **144**, 231–250, https://doi.org/10.1002/qj.3197.

Lebo, Z. J., H. Morrison, and J. H. Seinfeld, 2012: Are simulated aerosol-induced effects on deep convective clouds strongly dependent on saturation adjustment? *Atmos. Chem. Phys.*, **12**, 9941–9964, https://doi.org/10.5194/acp-12-9941-2012.

Manzato, A., 2003: A climatology of instability indices derived from Friuli Venezia Giulia soundings, using three different methods. *Atmos. Res.*, **67–68**, 417–454, https://doi.org/10.1016/S0169-8095(03)00058-9.

——, 2012: Hail in Northeast Italy: Climatology and bivariate analysis with the sounding-derived indices. *J. Appl. Meteor. Climatol.*, **51**, 449–467, https://doi.org/10.1175/JAMC-D-10-05012.1.

——, 2013: Hail in northeast Italy: A neural network ensemble forecast using sounding-derived indices. *Wea. Forecasting*, **28**, 3–28, https://doi.org/10.1175/WAF-D-12-00034.1.

Markowski, P. M., and Y. P. Richardson, 2010: *Mesoscale Meteorology in Midlatitudes*. 1st ed. Wiley-Blackwell, 407 pp.

Marwitz, J. D., 1972: The structure and motion of severe hailstorms. Part I: Supercell storms. *J. Appl. Meteor.*, **11**, 166–179, https://doi.org/10.1175/1520-0450(1972)011<0166:TSAMOS>2.0.CO;2.

McCaul, E. W., and M. L. Weisman, 2001: The sensitivity of simulated supercell structure and intensity to variations in the shapes of environmental buoyancy and shear profiles. *Mon. Wea. Rev.*, **129**, 664–687, https://doi.org/10.1175/1520-0493(2001)129<0664:TSOSSS>2.0.CO;2.

——, and C. Cohen, 2002: The impact on simulated storm structure and intensity of variations in the mixed layer and moist layer depths. *Mon. Wea. Rev.*, **130**, 1722–1748, https://doi.org/10.1175/1520-0493(2002)130<1722:TIOSSS>2.0.CO;2.

——, ——, and C. Kirkpatrick, 2005: The sensitivity of simulated storm structure, intensity, and precipitation efficiency to environmental temperature. *Mon. Wea. Rev.*, **133**, 3015–3037, https://doi.org/10.1175/MWR3015.1.

Miller, L. J., and J. C. Fankhauser, 1983: Radar echo structure, air motion and hail formation in a large stationary multicellular thunderstorm. *J. Atmos. Sci.*, **40**, 2399–2418, https://doi.org/10.1175/1520-0469(1983)040<2399:RESAMA>2.0.CO;2.

——, J. D. Tuttle, and C. A. Knight, 1988: Airflow and hail growth in a severe northern high plains supercell. *J. Atmos. Sci.*, **45**, 736–762, https://doi.org/10.1175/1520-0469(1988)045<0736:AAHGIA>2.0.CO;2.

Mitchell, D. L., and A. J. Heymsfield, 2005: Refinements in the treatment of ice particle terminal velocities, highlighting aggregates. *J. Atmos. Sci.*, **62**, 1637–1644, https://doi.org/10.1175/JAS3413.1.

Morrison, H., 2016a: Impacts of updraft size and dimensionality on the perturbation pressure and vertical velocity in cumulus convection: Part I: Simple, generalized analytic solutions. *J. Atmos. Sci.*, **73**, 1441–1454, https://doi.org/10.1175/JAS-D-15-0040.1.

——, 2016b: Impacts of updraft size and dimensionality on the perturbation pressure and vertical velocity in cumulus convection: Part II: Comparison of theoretical and numerical solutions and fully dynamical simulations. *J. Atmos. Sci.*, **73**, 1455–1480, https://doi.org/10.1175/JAS-D-15-0041.1.

——, J. A. Curry, and V. I. Khvorostyanov, 2005: A new double-moment microphysics parameterization for application in cloud and climate models. Part I: Description. *J. Atmos. Sci.*, **62**, 1665–1677, https://doi.org/10.1175/JAS3446.1.

——, G. Thompson, and V. Tatarskii, 2009: Impact of cloud microphysics on the development of trailing stratiform precipitation in a simulated squall line: Comparison of one- and two-moment schemes. *Mon. Wea. Rev.*, **137**, 991–1007, https://doi.org/10.1175/2008MWR2556.1.

——, J. A. Milbrandt, G. H. Bryan, K. Ikeda, S. A. Tessendorf, and G. Thompson, 2015: Parameterization of cloud microphysics based on the prediction of bulk ice particle properties. Part II: Case study comparisons with observations and other schemes. *J. Atmos. Sci.*, **72**, 312–339, https://doi.org/10.1175/JAS-D-14-0066.1.

——, J. M. Peters, A. C. Varble, W. M. Hannah, and S. E. Giangrande, 2020: Thermal chains and entrainment in cumulus updrafts. Part I: Theoretical description. *J. Atmos. Sci.*, **77**, 3637–3660, https://doi.org/10.1175/JAS-D-19-0243.1.

Murdzek, S., P. Markowski, Y. Richardson, and M. R. Kumjian, 2021: Should reversible convective inhibition be used when determining the inflow layer of a convective storm? *J. Atmos. Sci.*, **78**, 3047–3067, https://doi.org/10.1175/JAS-D-21-0069.1.

National Weather Service-San Antonio, 2016: Weather event summary: San Antonio April 12, 2016. NOAA/NWS, 5 pp., https://www.weather.gov/media/ewx/wxevents/ewx-20160412.pdf.

National Weather Service WDTB, 2021: Warning operations course (WOC): Severe track. Online Training, accessed 2 November 2020, https://training.weather.gov/wdtd/courses/woc/severe.php.

Nelson, S. P., 1983: The influence of storm flow structure on hail growth. *J. Atmos. Sci.*, **40**, 1965–1983, https://doi.org/10.1175/1520-0469(1983)040<1965:TIOSFS>2.0.CO;2.

——, 1987: The hybrid multicellular-supercellular storm—An efficient hail producer. Part II: General characteristics and implications for hail growth. *J. Atmos. Sci.*, **44**, 2060–2073, https://doi.org/10.1175/1520-0469(1987)044<2060:THMSEH>2.0.CO;2.

Nowotarski, C. J., J. M. Peters, and J. P. Mulholland, 2020: Evaluating the effective inflow layer of simulated supercell updrafts. *Mon. Wea. Rev.*, **148**, 3507–3532, https://doi.org/10.1175/MWR-D-20-0013.1.

Ortega, K. L., 2018: Evaluating multi-radar, multi-sensor products for surface hailfall diagnosis. *Electron. J. Severe Storms Meteor.*, **13** (1), https://ejssm.org/archives/2018/vol-13-1-2018/.

Paluch, I. R., 1978: Size sorting of hail in a three-dimensional updraft and implications for hail suppression. *J. Appl. Meteor. Climatol.*, **17**, 763–777, https://doi.org/10.1175/1520-0450(1978)017<0763:SSOHIA>2.0.CO;2.

Peters, J. M., 2016: The impact of effective buoyancy and dynamic pressure forcing on vertical velocities within two-dimensional updrafts. *J. Atmos. Sci.*, **73**, 4531–4551, https://doi.org/10.1175/JAS-D-16-0016.1.

——, and D. R. Chavas, 2021: Evaluating the conservation of energy variables in simulations of deep moist convection. *J.*

Atmos. Sci., **78**, 3229–3246, https://doi.org/10.1175/JAS-D-20-0351.1.

——, C. J. Nowotarski, and H. C. Morrison, 2019: The role of vertical wind shear in modulating maximum supercell updraft velocities. *J. Atmos. Sci.*, **76**, 3169–3189, https://doi.org/10.1175/JAS-D-19-0096.1.

——, H. Morrison, C. J. Nowotarski, J. P. Mulholland, and R. L. Thompson, 2020a: A formula for the maximum vertical velocity in supercell updrafts. *J. Atmos. Sci.*, **77**, 3747–3757, https://doi.org/10.1175/JAS-D-20-0103.1.

——, C. J. Nowotarski, and G. L. Mullendore, 2020b: Are supercells resistant to entrainment because of their rotation? *J. Atmos. Sci.*, **77**, 1475–1495, https://doi.org/10.1175/JAS-D-19-0316.1.

Picca, J. C., and A. V. Ryzhkov, 2012: A dual-wavelength polarimetric analysis of the 16 May 2010 Oklahoma City extreme hailstorm. *Mon. Wea. Rev.*, **140**, 1385–1403, https://doi.org/10.1175/MWR-D-11-00112.1.

Poolman, E. R., 1992: Die voorspelling van haelkorrelgroei in Suid-Afrika (the forecasting of hail growth in South Africa). M.S. thesis, Faculty of Engineering, University of Pretoria, 113 pp.

Pruppacher, H. R., and J. D. Klett, 1997: *Microphysics of Clouds and Precipitation*. 2nd ed. Kluwer Academic Publishers, 954 pp.

Púčik, T., P. Groenemeijer, D. Rýva, and M. Kolář, 2015: Proximity soundings of severe and nonsevere thunderstorms in Central Europe. *Mon. Wea. Rev.*, **143**, 4805–4821, https://doi.org/10.1175/MWR-D-15-0104.1.

Rasmussen, E. N., and D. O. Blanchard, 1998: A baseline climatology of sounding-derived supercell and tornado forecast parameters. *Wea. Forecasting*, **13**, 1146–1164, https://doi.org/10.1175/1520-0434(1998)013<1148:ABCOSD>2.0.CO;2.

Rasmussen, R. M., and A. J. Heymsfield, 1987: Melting and shedding of graupel and hail. Part III: Investigation of the role of shed drops as hail embryos in the 1 August CCOPE severe storm. *J. Atmos. Sci.*, **44**, 2783–2803, https://doi.org/10.1175/1520-0469(1987)044<2783:MASOGA>2.0.CO;2.

Renick, J. H., and J. B. Maxwell, 1977: Forecasting hailfall in Alberta. *Hail: A Review of Hail Science and Hail Suppression*, S. W. Borland et al., Eds., Amer. Meteor. Soc., 145–154.

Romps, D. M., 2015: MSE minus CAPE is the true conserved variable for an adiabatically lifted parcel. *J. Atmos. Sci.*, **72**, 3639–3646, https://doi.org/10.1175/JAS-D-15-0054.1.

Sherburn, K. D., and M. D. Parker, 2014: Climatology and ingredients of significant severe convection in high-shear, low-CAPE environments. *Wea. Forecasting*, **29**, 854–877, https://doi.org/10.1175/WAF-D-13-00041.1.

Skamarock, W. C., and Coauthors, 2008: A description of the Advanced Research WRF version 3. NCAR Tech. Note NCAR/TN-475+STR, 113 pp., https://doi.org/10.5065/D68S4MVH.

Smith, B. T., R. L. Thompson, J. S. Grams, C. Broyles, and H. E. Brooks, 2012: Convective modes for significant severe thunderstorms in the contiguous United States. Part I: Storm classification and climatology. *Wea. Forecasting*, **27**, 1114–1135, https://doi.org/10.1175/WAF-D-11-00115.1.

Tang, B. H., V. A. Gensini, and C. R. Homeyer, 2019: Trends in United States large hail environments and observations. *npj Climate Atmos. Sci.*, **2**, 45, https://doi.org/10.1038/s41612-019-0103-7.

Taszarek, M., H. E. Brooks, and B. Czernecki, 2017: Sounding-derived parameters associated with convective hazards in Europe. *Mon. Wea. Rev.*, **145**, 1511–1528, https://doi.org/10.1175/MWR-D-16-0384.1.

——, J. T. Allen, T. Púčik, K. A. Hoogewind, and H. E. Brooks, 2020: Severe convective storms across Europe and the United States. Part II: ERA5 environments associated with lightning, large hail, severe wind, and tornadoes. *J. Climate*, **33**, 10 263–10 286, https://doi.org/10.1175/JCLI-D-20-0346.1.

Tessendorf, S. A., L. J. Miller, K. C. Wiens, and S. A. Rutledge, 2005: The 29 June supercell observed during STEPS. Part I: Kinematics and microphysics. *J. Atmos. Sci.*, **62**, 4127–4150, https://doi.org/10.1175/JAS3585.1.

Thompson, R. L., R. Edwards, J. A. Hart, K. L. Elmore, and P. Markowski, 2003: Close proximity soundings within supercell environments obtained from the Rapid Update Cycle. *Wea. Forecasting*, **18**, 1243–1261, https://doi.org/10.1175/1520-0434(2003)018<1243:CPSWSE>2.0.CO;2.

Trapp, R. J., G. R. Marion, and S. W. Nesbitt, 2017: The regulation of tornado intensity by updraft width. *J. Atmos. Sci.*, **74**, 4199–4211, https://doi.org/10.1175/JAS-D-16-0331.1.

Warren, R. A., H. Richter, H. A. Ramsay, S. T. Siems, and M. J. Manton, 2017: Impact of variations in upper-level shear on simulated supercells. *Mon. Wea. Rev.*, **145**, 2659–2681, https://doi.org/10.1175/MWR-D-16-0412.1.

Weisman, M. L., and J. B. Klemp, 1982: The dependence of numerically simulated convective storms on vertical wind shear and buoyancy. *Mon. Wea. Rev.*, **110**, 504–520, https://doi.org/10.1175/1520-0493(1982)110<0504:TDONSC>2.0.CO;2.

——, and R. Rotunno, 2000: The use of vertical wind shear versus helicity in interpreting supercell dynamics. *J. Atmos. Sci.*, **57**, 1452–1472, https://doi.org/10.1175/1520-0469(2000)057<1452:TUOVWS>2.0.CO;2.

Witt, A., N. D. Eilts, G. J. Stumpf, J. T. Johnson, E. D. Mitchell, and K. W. Thomas, 1998: An enhanced hail detection algorithm for the WSR-88D. *Wea. Forecasting*, **13**, 286–303, https://doi.org/10.1175/1520-0434(1998)013<0286:AEHDAF>2.0.CO;2.

Ziegler, C. L., P. S. Ray, and N. C. Knight, 1983: Hail growth in an Oklahoma multicell storm. *J. Atmos. Sci.*, **40**, 1768–1791, https://doi.org/10.1175/1520-0469(1983)040<1768:HGIAOM>2.0.CO;2.